J. Fluid Mech. (2005), *vol.* 532, *pp.* 1–52.
doi:10.1017/S0022112005003733 Printed in the United Kingdom

Progressive waves with persistent two-dimensional surface patterns in deep water

By JOSEPH L. HAMMACK[1], DIANE M. HENDERSON[1] AND HARVEY SEGUR[2]

[1]William G. Pritchard Fluid Mechanics Laboratory, Department of Mathematics, Penn State University, University Park, PA 16802, USA

[2]Department of Applied Mathematics, University of Colorado, Boulder, CO 80309-0526, USA

(Received 3 November 2003 and in revised form 23 November 2004)

Experiments are conducted to generate progressive wave fields in deep water with two-dimensional surface patterns for which two parameters are systematically varied: (i) the aspect ratio of the cells comprising the surface patterns and (ii) a measure of nonlinearity of the input wave field. The goal of these experiments is to determine whether these patterns persist, what their main features are, whether standard models of waves describe these features, and whether there are parameter regimes in which the patterns are stable. We find that in some parameter regimes, surface patterns in deep water do persist with little change of form during the time of the experiment. In other parameter regimes, particularly for large-amplitude experiments, the patterns evolve more significantly. We characterize the patterns and their evolutions with a list of observed features. To describe the patterns and features, we consider two models: (*a*) the standard $(2+1)$ nonlinear Schrödinger equation and (*b*) coupled nonlinear Schrödinger equations for two interacting wavetrains. Exact solutions of these models provide qualitative explanations for many of the observed features.

1. Introduction

Herein we present experiments on laboratory-generated, progressive waves with two-dimensional surface patterns (and three-dimensional velocity fields) in deep water. Figure 1 shows a typical surface pattern: it has a non-trivial, periodic structure in two horizontal dimensions, and it propagates with little apparent change of form, at least in the length of the wavetank. Persistent, spatial structure such as the one shown here may have useful consequences in the study and description of deep-water waves. Thus, the purpose of this paper is to explore these two-dimensional surface patterns in deep water. What are their main features? Which of their features can be explained in terms of standard theories, and which cannot? Are these surface patterns ever stable? If so, under what conditions?

This investigation is a more detailed and extensive study of experiments reported by Hammack & Henderson (2003). We use a wavemaker array, described in § 2, comprising 32 individual paddles, each controlled precisely to perform a prescribed vertical displacement with a prescribed velocity. Two types of wavemaker forcings are used to generate two-dimensional surface patterns: (i) two symmetric carrier waves interacting at an oblique angle and (ii) a single carrier wave with a Jacobi elliptic sine function modulation in the transverse direction. Experiments are conducted using a range of two parameters: (i) a measure of two-dimensionality (aspect ratio) and (ii) a

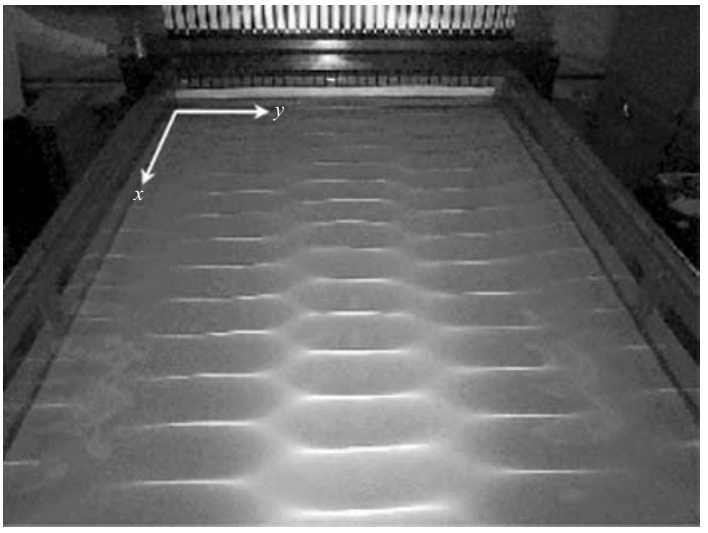

FIGURE 1. A typical bi-periodic pattern of progressive surface waves in deep water.

measure of nonlinearity (wave steepness). Data are presented from overhead images and from time series obtained by traversing wave-gauges at constant speeds through surface patterns along directions that are either parallel or perpendicular to the direction of pattern propagation. From these data, we catalogue twelve qualitative features of the surface patterns, based on our observations. A summary of these features follows.

In some parameter regimes the patterns evolve with only small changes in form. Some features of these slowly evolving patterns are that:

(i) Unlike the two-dimensional patterns that propagate as waves of permanent form in shallow water, where the cells are observed to be six-sided, the surface patterns that we observe in deep water comprise primarily rectangular four-sided cells. Two of the sides are nodal lines of zero surface displacement parallel to the axis of propagation and common to all cells in that row, as in the pattern shown in figure 1.

(ii) Crests parallel to the wavemaker array may be flat or may have a dip in their centre. (For example, the crests in figure 1 appear relatively flat over a large fraction of each periodic cell.)

(iii) For some experiments with large nonlinearity, cells appear to pinch in half.

(iv) In some experiments, the crests parallel to the wavemaker array curved.

We will show that all of these features can be explained using standard theories. In particular, we review the derivation of the standard nonlinear Schrödinger equation and present a derivation of two coupled nonlinear Schrödinger equations in § 5.1. We show that the appropriate exact solutions of these two models, used in a third-order expansion of the water surface displacement, exhibit the features listed above.

In other parameter regimes the patterns evolve more significantly. Some features of this evolution are that:

(v) Wave envelopes exhibit modulations in the x-direction with frequencies that depend on aspect ratio. (The x-direction is in the direction of wave-pattern propagation and is shown in the photograph of the wave basin in figure 1.)

(vi) For some experiments with large nonlinearity, the width of the nodal line region varies as the wave propagates.

(vii) A region of non- zero surface displacement develops within the region of nodal lines in the most nonlinear experiments and in many of the experiments using the elliptic function forcing.

(viii) Small-scale structures may develop on the larger pattern.

(ix) A connecting leg between cells may develop. These legs are narrow regions of non-zero surface displacement that traverse the nodal line to connect two adjoining cells.

To describe these unsteady features, we discuss ongoing work on the stability of the exact solutions mentioned above, and how they apply to the experiments.

There is extensive literature on theory and experiments for surface patterns of waves in shallow water. In this regime, waves that propagate with permanent form and with two-dimensional periodic surface patterns are observed experimentally (Hammack *et al.* 1989, 1991, 1995), are found in approximate models (Segur & Finkel 1985), and have been proved to exist in the classic boundary-value problem for water waves (Craig & Nicholls 2000).

A main difference between the shallow- and deep-water regimes is that according to classic stability results (e.g. Benjamin & Feir 1967; Whitham 1967), uniform trains of plane (i.e. one-dimensional) waves are known to be unstable in deep water, but not in shallow water. A consequence of this instability is that two-dimensional surface wave patterns might also be unstable in deep water, and so might not persist long enough to be physically relevant. This classic result has been questioned by Segur *et al.* (2005), who showed that dissipation stabilizes the underlying wavetrain. Regardless of stability/instability, there has long been interest in two-dimensional surface patterns that propagate as waves of permanent form in deep water.

Permanent-form solutions with two-dimensional patterns have been observed in numerical computations for waves in deep water by Roberts (1983), Roberts & Peregrine (1983), Roberts & Schwartz (1983), Bryant (1985), Nicholls (1998), Craig & Nicholls (2000) and others. The existence proof for permanent-form waves with two-dimensional surface patterns by Craig & Nicholls (2000) is for waves in water of arbitrary depth, so it applies to waves on deep water. Previous experiments have also shown persistent patterns of two-dimensional waves on deep water. Su (1982) and Su *et al.* (1982) found at least two types of wave with two-dimensional surface patterns. Figure 4 of Su (1982) shows one, a transient 'skew wave pattern' that resembles the patterns found in the numerics discussed above. The second type, referred to as 'crescent waves' or 'horseshoe' patterns, has also been observed experimentally by Caulliez, Ricci & Dupont (1998) and Collard & Caulliez (1999). These patterns resulted from two-dimensional instabilities of one-dimensional wavetrains. Kimmoun, Branger & Kharif (1999) used a single long wavepaddle to create a one-dimensional wavetrain that reflected off a wall. The interaction between the incident and reflecting waves resulted in patterns whose contour maps look rectangular, like the patterns we describe herein. Caulliez & Collard (1999) generated wave fields with wind and listed five distinct regimes of qualitative behaviour, each of which was characterized by different types of wave patterns. Some of these wind-wave patterns were rhombi, hexagons and pentagons. The rhombi patterns, most similar to what we observe here, resulted either from quasi-monochromatic wave fields, which were the initial waves that grew from the wind and that interacted obliquely, or developed from a seemingly random field of gravity–capillary waves.

In our opinion, two-dimensional patterns of waves in deep water are of scientific interest because some patterns, such as the one shown in figure 1, persist over moderately long distances. This persistence indicates that even if perturbations grow,

they leave the overall pattern largely intact. Unfortunately, the test section of our experimental facility is not very long, and we have not yet resolved questions of stability of these patterns with definitive experiments. We regard the persistence and stability of the wave patterns examined in this paper as major open questions.

An outline of the remainder of the paper is as follows. Section 2 presents a description of the experimental facility and procedures. Section 3 discusses the detailed shape of the wave patterns we observe in deep water. Section 4 presents results of two different sets of experiments. The first used two symmetric carrier waves interacting at oblique angles. The second used a carrier wave propagating in the x-direction that had a Jacobi elliptic sine function modulation in the y-direction. A summary of the observations is given in § 5, where the nonlinear Schrödinger (NLS) models are provided and a qualitative comparison of the experiments with theoretical explanations that use the NLS framework is given. In the current formulation of these models, we consider gravity-driven waves on an inviscid fluid. For simplicity both surface tension and wave dissipation are neglected. A final overview is given in § 5.3.

2. Experimental facility and approach

Experiments are conducted in a wave basin that is 12 ft long, 6 ft wide and 1 ft deep, with an undisturbed water depth of $h = 20$ cm. The basin has precisely aligned glass walls and a flat bottom made of (white) Corian (from Dupont). Along one 6 ft endwall is a segmented wavemaker comprising 32, side-by-side, vertically oscillating triangular wedges (paddles) that intersect the water surface. There are no gaps between adjacent paddles – each paddle touches its neighbour. The 32 paddles do not touch the tank's endwall, but are less than 0.5 mm away from it so as to inhibit flow from behind the paddles. The motion of each paddle is independently programmable and controlled by dedicated real-time computers using dual feedbacks from each paddle. (Dual feedbacks of position and velocity enable the most precise control available today.) The segmented wavemaker can generate complex wave fields comprising multiple waves propagating at arbitrary angles. It can be programmed to modulate wave fields with any desired functional dependence in both the x (along basin) and the y (across basin) directions. The basin has a programmable, controlled, x, y, z-positioning system that rides over the basin; it is used to support wave gauges that may be at rest or may traverse the tank at any desired angle and speed. In addition, there is an overhead high-resolution CCD imager whose x-motion along the basin centreline is also programmable and feedback controlled. The real-time computers controlling the wavemaker, the x, y, z-positioning system, and the imager positioning systems are all synchronized.

In each experiment discussed herein, we control frequency, amplitude and the y-wavelength. Then, the x-wavelength is a derived parameter as described below. All of the paddles oscillate vertically at the same frequency for that experiment, each with a different amplitude given by that experiment. We used the frequency in the linear dispersion relationship for gravity waves, $\omega^2 = g\kappa$, to obtain the wavenumber, κ. Throughout this paper, we neglect the effects of surface tension based on the smallness of the Bond number, $T\kappa^2/g$, where T is the kinematic surface tension and g is the acceleration due to gravity. In the experiments presented herein, the Bond number, which measures the relative importance of surface tension and gravitational forces, varies from 0.01 to 0.07. We then chose the y-wavelength and computed the x-wavelength from κ to correspond to one of the two types of wavemaker forcings used. For a desired wave amplitude, a_0, we oscillate the paddle at a_0/C, where C is a

Experiment	n	ρ	l	k
C1	0	0	0	0.64
C2	2	0.11	0.034	0.64
C3	3	0.16	0.051	0.64
C4	4	0.21	0.069	0.64
C5	5	0.27	0.086	0.64
C6	6	0.32	0.10	0.64
C7	7	0.38	0.12	0.63
C8	8	0.44	0.14	0.63

TABLE 1. Parameters for experiments using the linear superpostion of two cosines as in (1), for which the aspect ratio was varied while a measure of nonlinearity was held fixed. The frequency of the carrier waves for all of the experiments was 4.00 Hz. The wavenumber for all of the above experiments was $\kappa = 0.64\,\mathrm{cm}^{-1}$. The amplitude for all waves was $a_0 = 0.32\,\mathrm{cm}$, so that $a_0\kappa = 0.20$.

calibration constant determined by experimentally looking at the one-dimensional wavemaker problem for the triangular-shaped plunger (Pritt 2003). For forcing frequencies of 3.33 Hz, $C = 0.74$. For forcing frequencies of 4 and 5 Hz, $C = 0.79$.

For all experiments discussed herein, the spatial structure of the wave fields in the y-direction was chosen so that the tank sidewalls were located at lines of symmetry of the wave fields. There was no beach at the end of the tank. The experiments were conducted for the short time available (about 20 s) before reflections from the endwall occurred.

The first type of forcing used two symmetric one-dimensional plane waves, each at an oblique angle, so the displacement of the jth paddle ($1 \leqslant j \leqslant 32$) was given by

$$\eta_{pj} = \tfrac{1}{2}a_0 \cos(kx + ly_j - \omega t) + \tfrac{1}{2}a_0 \cos(kx - ly_j - \omega t) = a_0 \cos(ly_j)\cos(kx - \omega t), \quad (1)$$

with y_j corresponding to the y-location of the middle of the jth paddle, and with $x = 0$. The velocities of the wave paddles were obtained by using a similarly digitized version of the time-derivative of (1). This forcing function represents a wave propagating in the x-direction with an amplitude variation in y that is approximately sinusoidal. It achieves the goal of creating a two-dimensional surface pattern near the wavemaker, and this pattern may then propagate down the tank in the x-direction. The forced patterns are rectangular cells with an x-length corresponding to the x-wavelength, $L_x = 2\pi/k$, of the carrier waves and a y-length scale corresponding to half the y-wavelength, $L_y = 2\pi/l$, of the carrier waves with $\kappa = \sqrt{k^2 + l^2}$. Since the y-dependence has to have antinodes at the tank sidewalls, $l = n\pi/W$, where $W = 182.88\,\mathrm{cm}$ is the tank width and n is the number of nodal lines (parallel to the x-axis) across the tank. If the actual patterns for all x and y looked like those given by the forcing in (1), then the water-suface displacement in the nodal lines would be constant for all x. This type of forcing was used for fourteen experiments presented herein, in which either the aspect ratio, $\rho = 2L_x/L_y$, or the nonlinearity, $a_0\kappa$ was varied. The parameters for each experiment are given in tables 1 and 2.

The second type of forcing used a carrier wave propagating in the x-direction that was modulated in the y-direction with a Jacobi elliptic sine function, so that the displacement of the jth paddle was given by:

$$\eta_{pj} = a_0 \,\mathrm{sn}[c(y_j + y_0), m]\cos(kx - \omega t), \quad (2)$$

with y_j corresponding to the y-location of the middle of the jth paddle, and with

Experiment	a_0 (cm)	$a_0\kappa$
C9	0.24	0.15
C10	0.32	0.20
C11	0.39	0.25
C12	0.47	0.30
C13	0.55	0.35
C14	0.63	0.40

TABLE 2. Parameters for experiments using the linear superpostion of two cosines as in (1), for which a measure of nonlinearity was varied while the aspect ratio was held fixed. The frequency of the carrier waves for all of the experiments was 4.00 Hz. The wavenumber for all of the above experiments was $\kappa = 0.64\,\mathrm{cm}^{-1}$. The y-wavenumber for all waves was $0.10\,\mathrm{cm}^{-1}$, corresponding to a mode $n = 6$ wave field, for which $\rho = 0.33$. (We note that experiments C6 and C10 are the same experiment.)

Exp	f (Hz)	a_0 (cm)	k (cm^{-1})	c (cm^{-1})	m	a_0k	ρ	n
Sn1	4.00	0.25	0.64	0.0625	0.9717	0.16	0.11	2
Sn2	4.00	0.50	0.64	0.122	0.9952	0.32	0.16	3
Sn3	4.00	0.50	0.64	0.125	0.9717	0.32	0.21	4
Sn4	4.00	0.35	0.64	0.0885	0.9603	0.22	0.16	3
Sn5	5.00	0.35	1.01	0.294	0.9900	0.35	0.29	8
Sn6	3.33	0.40	0.45	0.0347	0.9819	0.18	0.08	1

TABLE 3. Parameters for experiments using a carrier wave and Jacobi elliptic sine modulation along the paddle array as in (2).

$x = 0$. Here, $\kappa = k$ and m is called the elliptic modulus. (Several notations are available. For example, our m is denoted k by Byrd & Friedman 1971.) The shift in y-axis, $y_0 = \mathrm{K}(m)/c$, where K is the elliptic integral of the first kind, ensures the wave had an antinode at the wall. The velocities of the wave paddles were obtained by using a similarly digitized version of the time-derivative of (2). The resulting rectangular pattern has an x-length scale that corresponds to the x-wavelength of the carrier wave, $L_x = 2\pi/k$, and a y-length that corresponds to half the y-period given by the Jacobi elliptic sine modulation. The y-wavelength imposed by the modulation is $L_y = 4\mathrm{K}(m)/c$. The parameters used in (2) for the six experiments considered here are given in table 3.

With either type of forcing, we used two methods to measure the waves. First, two capacitance-type wave gauges were supported above the basin using the x, y, z-positioning system. Each gauge measured the instantaneous water-surface displacement at a 'point' (a circular area of about 1 mm diameter). The positioning system enables the dynamic calibration of these gauges as well as their precise positioning and motion across the water surface during experiments. In particular, we used the positioning system to traverse the gauges across the tank in one of two directions, through the patterns at a constant speed of $v = 10.59\,\mathrm{cm\,s}^{-1}$. There are two kinds of traverse for each experiment: (i) a traverse parallel to the y-axis at speed v, with fixed x-locations of 50 and 100 cm from the wavemaker; and (ii) a traverse parallel to the x-axis at speed v, with fixed y-locations chosen to be in the center of the crest-region of the pattern and in a nodal line of the pattern. The analogue signals from the gauges were low-pass (30 Hz) filtered, amplified and digitized with 16-bit accuracy using another synchronized real-time computer.

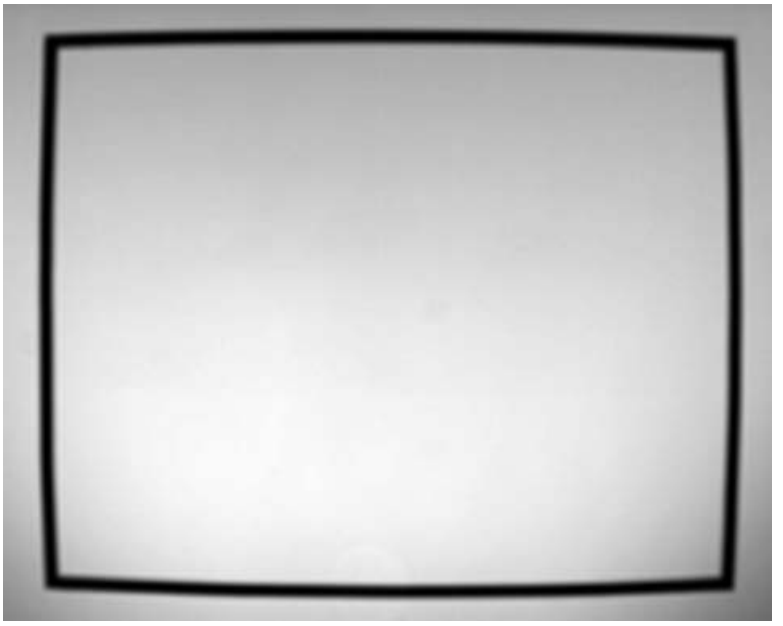

FIGURE 2. Image of a rectangle with outside dimensions 100 cm × 75 cm made with tape mounted on the bottom of the wavetank covered by 20 cm of still water. The tape shows the slight curvature in the images due to lens distortion.

Secondly, instantaneous overhead images of the wave field were made using the overhead imager. Each image covers a surface area of 88.5 cm by 110.6 cm and comprises 8-bit grey levels recorded at 1.2 million pixels. An image of the wave field was produced on the Corian tank bottom by high-intensity lamps aimed obliquely at the water surface. Wave crests created light bands on the Corian and wave troughs created dark bands, as in figure 1. Previous work by Perlin & Hammack (1991) showed that a time series of grey levels at a pixel site has a correlation coefficient of about 0.89 with a nearby wave-gauge time series. Hence, we relate grey levels to water-surface displacements in discussions of the overhead images. In particular, we present the image of grey levels, the contour lines computed from these images, and the spatial, two-dimensional Fourier transforms computed from these images. There is some distortion in the images created by the lens of the imager. Figure 2 shows an image of a rectangle made with electrical tape mounted on the bottom of the tank under still water. It shows the resolution of the imager lens and the amount of curvature due to the lens distortion.

The experimental procedure was as follows:

1. The tank was filled with tap water to a 20 cm depth. Table 4 shows how many days the water had been in the tank on the day of each experiment.

2. The two gauges were dynamically calibrated by oscillating them at the carrier wave frequency with the water at rest. The calibrations were not linear; they were quadratic, and we used a separate calibration for water surface displacements above and below the still-water level.

3. With no waves present, the gauges were traversed along the x-axis at the given y-locations to obtain a time series of the level water surface (the 'x-level' time series). The reason for this step is to account for local variations in the capacitance field that are not due to the waves.

Experiment	Surface age (days)	δ (cm^{-1})
C1	2	0.010
C2	2	0.010
C3	2	0.010
C4	7	0.008
C5	7	0.008
C6	3	0.010
C7	2	0.011
C8	1	0.011
C9	2	0.008
C10	3	0.010
C11	2	0.008
C12	2	0.008
C13	0	0.000
C14	0	0.000
Sn1	1	0.003
Sn2	2	0.004
Sn3	2	0.004
Sn4	2	0.004
Sn5	0	0.000
Sn6	0	0.000

TABLE 4. Information on wave damping: the number of days after the tank was filled when the experiment was conducted and the decay rate of a one-dimensional 4 Hz wave measured on the day of the particular experiment.

4. The paddle array was programmed to oscillate as a single unit to create a one-dimensional 4 Hz wavetrain. The wave gauges traversed the tank in the x-direction to obtain a time series, which was used to obtain a decay rate for that experiment. To determine the decay rate, the time series obtained from the x-traverse through the one-dimensional wave fields (with the transient beginnings and ends cut off) was broken into 11 pieces of 3 s each that were overlapped at the midpoints. A measure of the energy in the time series is the L_2 norm of the surface elevation, $E = \int \eta(x - v\,t)^2\,\mathrm{d}(x - v\,t)$. We computed E for each piece of the time series in an experiment, and fit an exponential decay to the results. Table 4 gives the decay rate δ for each experiment, where δ is half the decay rate of E, such that amplitude a varies with distance from the wavemaker according to $a = a_0 \mathrm{e}^{-\delta x}$. Similar experiments using one-dimensional waves in a narrow tank (Segur *et al.* 2005) exhibited decay rates that increased with the age of the surface. Consistent with this result, the data in table 4 show that experiments conducted on the day the tank was filled had a very low decay rate. However, on subsequent days the decay rates did not correlate well with the age of the water surface, for which we have no explanation. Movies of waves on a surface with age 0 days compared to waves on a surface with an age of several days are at http:/www.math.psu.edu/dmh/FRG. The movies show the wave fields decaying faster on the water surfaces that were days old. They also show that small-scale instabilities develop and evolve further downstream of the paddles when the surface was fresh. In these experiments we did not clean the water surface. It is known that contaminants on the surface, which in these experiments may increase and change daily owing to fallout from the air and diffusion from the water, cause surface tension gradients, which affect various aspects of wave dynamics. See Miles (1967) for a model of surfactant effects on wave damping, Lucassen-Reynders & Lucassen (1969)

for a review of surfactant rheology and its effects on waves, and Liu & Duncan (2003) for results of experiments using surfactants and progressive waves.

5. The paddle array was programmed to make waves for a particular experiment. One gauge traversed the tank in the x-direction in two successive experiments: once for data in the crest-region and once for data in the nodal line. The x-level was subtracted from these data, and the result was calibrated. Since the wave-gauge was moving, the Fourier transform of the time series gives Doppler-shifted frequencies, f_d. To obtain the absolute frequencies we used

$$f = f_d \frac{c_p}{c_p - v}, \tag{3}$$

where c_p is the phase speed of the wave.

6. Two gauges traversed the tank in the y-direction simultaneously in one experiment at fixed $x = 50$ and 100 cm while the water surface was quiescent to obtain the time series for the level water in the y-direction (the 'y-level' time series).

7. The wave paddle was again oscillated according to the particular experiment. The two gauges at $x = 50$ and 100 cm were traversed across the tank in the y-direction to obtain the two y-traverse time series. The y-level time series was subtracted, and the result was calibrated.

8. With a still water surface (no waves), the carriage holding the overhead imager was programmed to move the imager at a speed $v = 10.59\,\mathrm{cm\,s^{-1}}$ along the centreline of the tank in the x-direction. It took images at one-second intervals. This sequence of images provided grey levels for the surface for the still-water case.

9. With the waves present, the overhead imager again traversed along the x-axis to obtain a sequence of images of the experiment. The grey levels from the level images were subtracted from the grey levels of the experiment images. In §§4.1 and 4.2, we show one image from these sequences for each experiment and the whole sequence for experiment C14. From these images we obtain contour maps and spatial Fourier transforms of the images. We do not use the grey levels to obtain quantitative values of wave amplitude.

We varied two parameters of the two-dimensional surface patterns shown here. The first parameter is a measure of nonlinearity, which we take to be $\epsilon := a_0\kappa$, where a_0 is the carrier wave amplitude(s) and $\kappa = \sqrt{k^2 + l^2}$ is the wavenumber. Recall that for the experiments using the Jacobi elliptic sine modulation, $l = 0$. The second parameter is the aspect ratio of the pattern. We define the aspect ratio to be $\rho := 2L_x/L_y$, where L_x is the x-wavelength of the pattern, and L_y is the y-wavelength of the pattern. So, in the experiments using oblique interactions of two carrier waves, $\rho = 2l/k$, as in (1). For experiments using a single carrier wave modulated in the y-direction with a Jacobi elliptic sine function, as in (2), $\rho = \pi c/(k\,\mathrm{K}(m))$, where c and m are given in table 3. In the remainder of the paper, we discuss experiments in which we varied ϵ and ρ for both types of experiments.

3. Surface patterns

It is known that permanent-form wavetrains with two-dimensional surface patterns in shallow water have a six-sided geometry with a zigzag structure connecting different cells (experiments: Hammack *et al.* 1989, 1991, 1995; approximate shallow-water models: Segur & Finkel 1985; and numerics: Craig & Nicholls 2002). Figure 3 shows two overhead photographs of an experiment in shallow water in which the pattern has a symmetric hexagonal shape. These patterns, symmetric or not, are well modelled by genus-2 solutions of the KP equation, an asymptotic evolution equation for

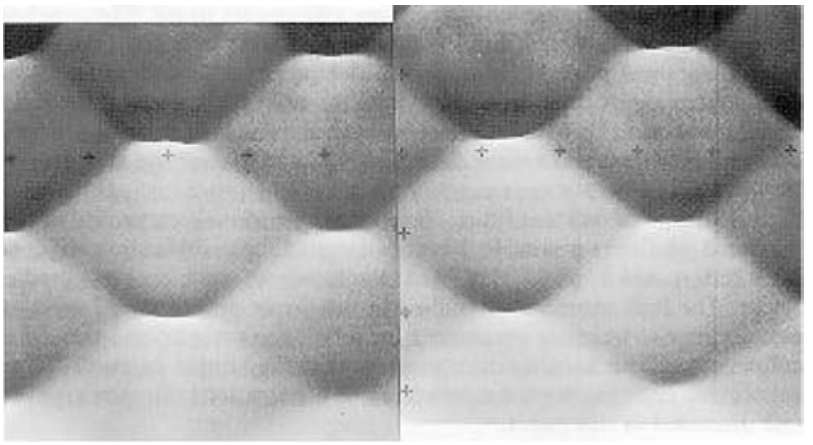

FIGURE 3. Overhead photograph of waves in shallow water (from Hammack *et al.* 1995).

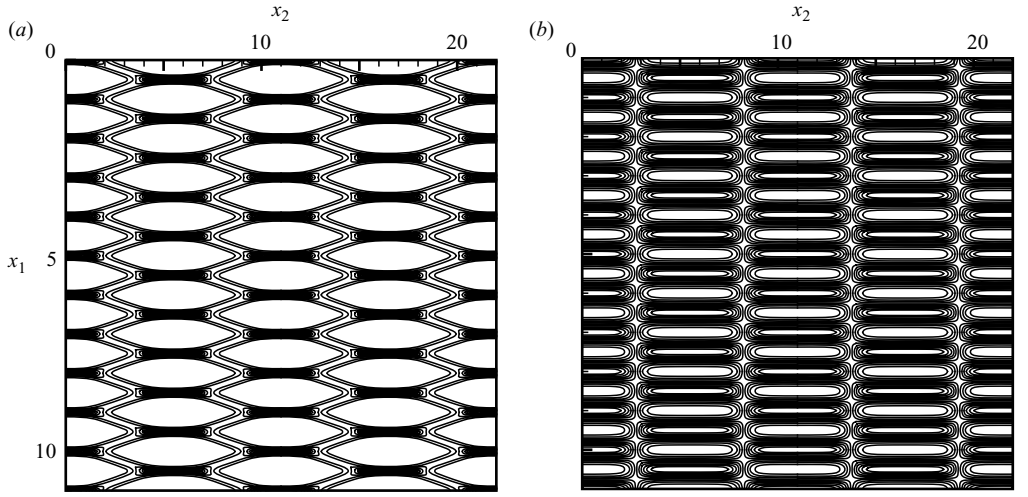

FIGURE 4. Numerically generated contours of travelling waves in (*a*) shallow and (*b*) deep water (Craig & Nicholls 2002.)

weakly nonlinear, weakly two-dimensional waves in shallow water (see for example, Hammack *et al.* 1989). Computations of the full nonlinear water wave equations by Craig & Nicholls (2002) confirm the hexagonal shape in shallow water, but show that patterns are quite different in deep water. Instead of the 6-sided (hexagonal) cells observed in shallow water, the cells in deep-water are 4-sided (rectangular) and have a straight nodal line separating cells, instead of the zigzag structure observed in shallow water. This difference is illustrated in figure 4, which shows contours of Craig & Nicholl's (2002) numerical solutions of the full boundary-value problem for waves in shallow and in deep water. In figure 4, the wave troughs are the white regions, and the steepest peaks are the darkest regions, with the most contour lines through them. Deep-water rectangular contours were observed experimentally by Kimmoun *et al.* (1999) in experiments using incident and reflected wavetrains.

A measurable difference between symmetric wave patterns of permanent form in shallow and deep water is seen in time-series taken in slices holding x_2 (our y) of

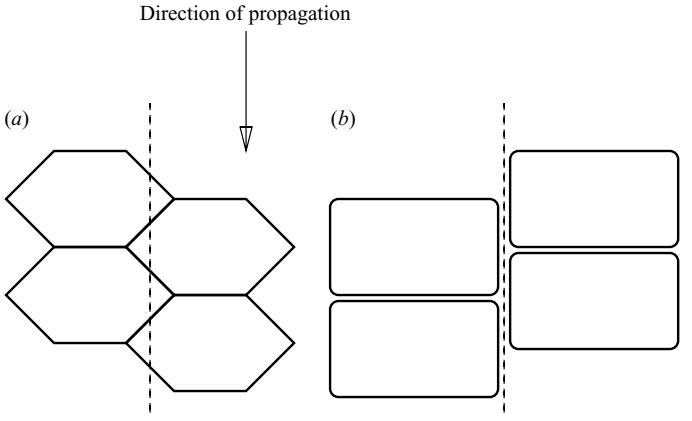

FIGURE 5. Schematic drawing of level lines for wave patterns corresponding to (*a*) hexagons in shallow water and (*b*) rectangles in deep water.

figure 4 fixed and varying x_1 (our x) through their respective patterns. In shallow water (figure 4*a*), the time series exhibits some temporal periodicity regardless of where the slice is obtained. The periodicity itself depends on where the slice is obtained. In deep water (figure 4*b*), there is a slice corresponding to the nodal line, along which the amplitude of the wave pattern vanishes. A schematic drawing of the level lines of patterns in shallow and deep water is shown in figure 5 to illustrate this difference. Measurements obtained through the patterns at a location indicated by the dashed lines have oscillations observed in the hexagons, but none observed in the nodal region of the rectangles. The oscillations observed in the hexagonal pattern have frequencies that depend on which slice is chosen. Measurements of time series in shallow water by Hammack *et al.* (1995) confirm this temporal behaviour for hexagonal patterns in shallow water.

Measurements of time series in our experiments, shown in §§4.1 and 4.2, confirm this temporal behaviour for rectangular patterns in deep water. From the images (also shown in §§4.1 and 4.2), it is difficult to determine whether the patterns are hexagonal, like those in figure 5(*a*), or rectangular, like those in figure 5(*b*). For example, the pattern in figure 1 may appear hexagonal to the eye. But our measurements with a wave-gauge that traverses in the x-direction in the nodal region (the region with the dashed line in figure 1*b*) prove that the pattern is rectangular; the time series in the nodal line for all x, such as those obtained from the experiment shown in figure 1, typically show a constant zero amplitude. This measurement is consistent with a nodal region of constant water-surface displacement in a rectangular pattern, rather than a zigzag region of periodic (with a different period from the carrier wave) displacement in a hexagonal pattern. We note that for some experiments, the scenario is not quite this simple; there are oscillations in some portions of the nodal region. However, the oscillations in these experiments grow downstream of the wavemaker and, more importantly, are always at the same frequency of the carrier wave. Thus, they cannot be due to a hexagonal cell structure. We discuss them further in §§4 and 5.

4. Experimental observations

In the remainder of the paper we discuss experiments in which we vary aspect ratio and nonlinearity for (i) the case of obliquely interacting symmetric waves and

Figure	Description	Experiment
6	Image. Contour map. Fourier transform	C1–C4
7	Image. Contour map. Fourier transform	C5–C8
8	Image. Contour map. Fourier transform	C9–C11
9	Image. Contour map. Fourier transform	C12–C14
10	x-time series	C1–C8
11	x-time series	C9–C14
12	y-time series	C1–C8
13	y-time series	C9–C14
14	Image. Contour map. Fourier transform	C14
15	Image. Contour map. Fourier transform	C14
16	Image. Contour map. Fourier transform	Sn1–Sn3
17	Image. Contour map. Fourier transform	Sn4–Sn6
18	y-time series	Sn1–Sn6
19	x-time series	Sn1–Sn6

TABLE 5. Figures that present data, the type of data and the experiment depicted.

Feature	Description	Experiment	Data
1	Persistence	C2–C11 Sn1, 2, 3, 4, 5, 6	Images
2	Rectangular cell geometry	C3–C10, Sn4, Sn6	x-time series in nodal region Contour maps of images
3	Connecting leg between cells	C2–C14, Sn1, Sn2, Sn3, Sn5	Contour maps of images
4	Oscillations in the nodal region	C2, C11–C14 Sn1, Sn2, Sn3, Sn5	x-time series in nodal region
5	Modulations in x-direction	All	x-time series in crest region
6	Small-scale waves	C1–C12, Sn1, Sn4	Images, Contour maps, y-time series
7	Pinch-off of cells	C2, C14	Images
8	Dips in crestlines in the y-direction	C2, C4, C12–C14 Sn2–Sn5	y-time series
9	Flattening of crestlines in the y-direction	C2–C14, Sn2–Sn5	y-time series
10	Time-varying width of the nodal region	C3, C4, C9, C11 Sn1, Sn2, Sn4, Sn5, Sn6	Contour maps of images
11	Zigzag structure	C14, Sn2	Contour maps of images
12	Curving of crestlines in the y-direction	C14, Sn2, 3, 4, 6	Images, Contour maps

TABLE 6. List of features observed in the data: a description of the feature; the experiments it appears in; which type of data was used to identify it.

(ii) the case of carrier waves modulated in the transverse direction with Jacobi elliptic sine functions. We present overhead images of the surface patterns and time series obtained by traversing the gauge in the x- and y-directions, as discussed in § 2. The data are presented in figures 6–19. Table 5 lists what type of data each figure shows and for what experiments.

In presenting the data, we point out several qualitative features that appear in one or more experiment. Table 6 has a brief description of each of these features, the experiments in which each was observed, and the type of data from which each was obtained.

4.1. *Obliquely interacting waves*

Here we consider experiments in which the wave paddle array was programmed to create an oblique interaction between two symmetric carrier waves as described by (1). Both the aspect ratio and nonlinearity were varied. Table 1 gives a description of experiments C1–C8, in which the nonlinearity was held constant at $a_0\kappa = 0.20$, and the aspect ratio was varied over $0 \leqslant \rho \leqslant 0.44$. This range corresponds to changing the number of nodal lines over $0 \leqslant n \leqslant 8$. In these experiments, the x-wavelength was held fixed, so the aspect ratio was varied by changing the y-wavelength of the patterns. The convention here is that a one-dimensional wave, like the one in experiment C1, has $\rho = 0$. An 'increasing' aspect ratio corresponds to a y-wavelength that decreases relative to the fixed x-wavelength. Table 2 gives parameters for experiments C9–C14, in which the aspect ratio was fixed at $\rho = 0.33$ ($n = 6$), and nonlinearity was varied over $0.15 \leqslant a_0\kappa \leqslant 0.40$. In these experiments, the nonlinearity was increased by increasing the amplitude, while holding the wavenumbers fixed.

Figures 6 and 7 show overhead images (column I) of wave fields (C1–C8) with fixed nonlinearity and varing aspect ratio, along with contour maps of the images (column II) and two-dimensional spatial Fourier transforms (column III) of the images. The contour maps and Fourier transforms are computed using the grey levels that comprise the images.

The centres of the images (column I) are 154 cm (about 15.4 wavelengths) from the wavemaker array. The cell patterns did not evolve significantly during that distance, and the patterns, for which there are about eight cells in the direction of propagation in each image, are essentially uniform throughout the images. The contour maps (column II) of the images show some evidence of evolution, which we discuss below. The Fourier transforms (column III) of the images show the imposed periodicity in the x- and y-directions as well as the harmonic of the input wave fields, but not the development of strong additional Fourier components.

This set of data shows that there are parameter regimes for which two-dimensional spatially periodic patterns in deep-water persist long enough to be observed in the wavetank. Whether or not the patterns would be stable 'enough' to persist throughout the length of the tank was not obvious *ab initio*, so we list persistence of patterns as the first feature in table 6. To determine a limit for this parameter regime in which there is persistence, we conducted experiments C9–C14, which had a fixed aspect ratio of $\rho = 0.33$ ($n = 6$) and varying nonlinearity, $a_0\kappa$. Figures 8 and 9 show images of the wave fields from these experiments, as well as the contour maps and Fourier transforms of the images. As the nonlinearity was increased, the cell patterns did begin to evolve within the x-interval shown in the image. In particular, the images (column I) of the most nonlinear experiments, C12–C14 ($0.30 \leqslant a_0\kappa \leqslant 0.40$), show differences in the cells at the tops and bottoms of the images.

A second feature of the cells (as listed in table 6 and discussed in § 3) is their geometries – are the cells hexagonal, rectangular or something else? It is difficult to determine the answer from the images. However, the contour maps of the images (column II) for experiments C2–C11 suggest that the cells look more like the computed rectangular patterns for deep-water shown in figure 4(b) than the computed hexagonal patterns for shallow-water shown in figure 4(a). Nevertheless, even the contour maps do not provide definitive information because of the presence of a diagonal 'connecting leg' (feature 3 in table 6) between some of the cells in all of the experiments C2–C14. The question of whether or not the nodal region shows a constant surface elevation is settled by obtaining time series from a gauge that has a fixed y-location in the

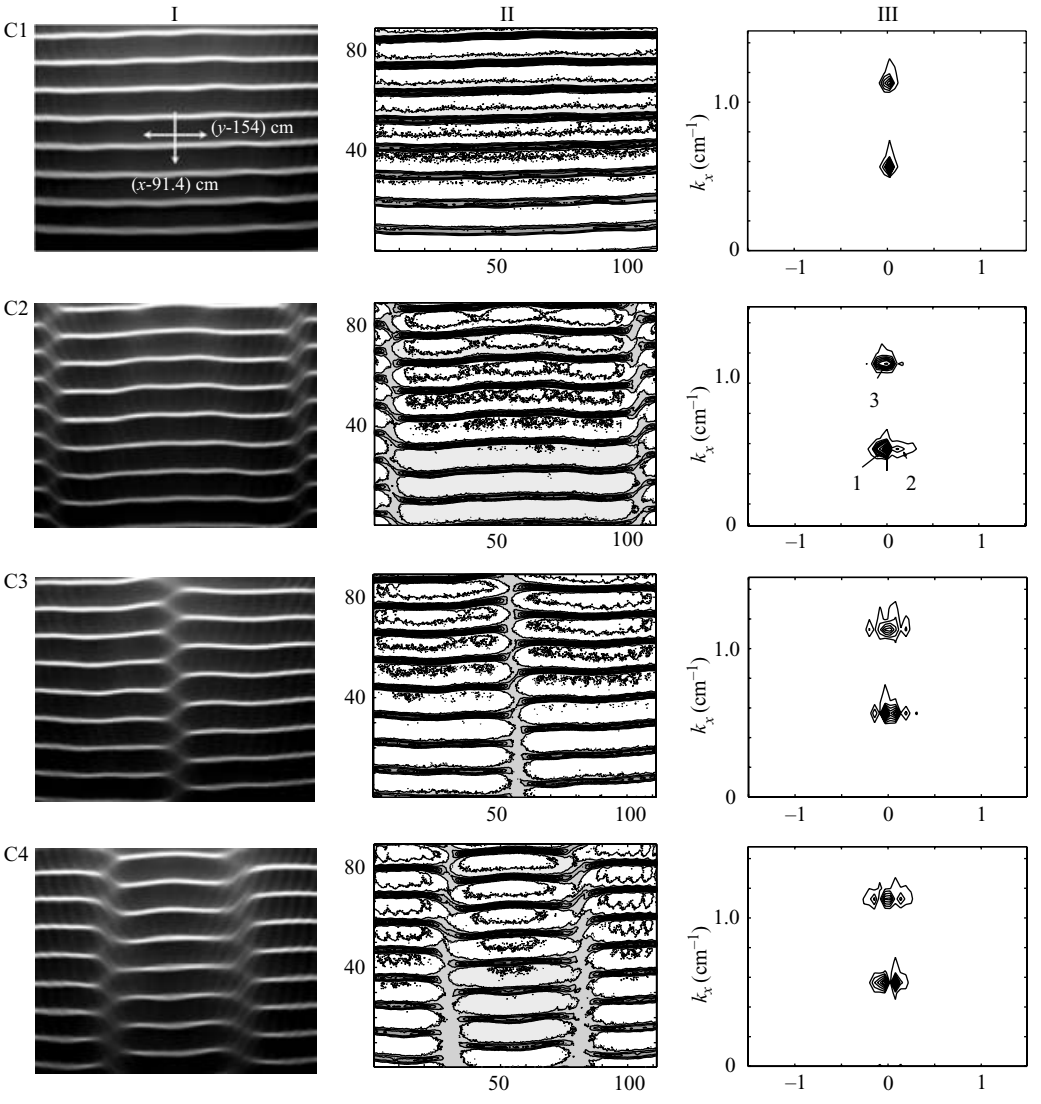

FIGURE 6. Images (column I), contour maps (column II) and spatial Fourier transforms (column III) of 4 Hz waves with $a_0\kappa = 0.20$ and $n = 0$, 2, 3, 4. Parameters for experiments C1–C4 are given in table 1. Surface patterns propagate from top to bottom of the image. The origin of the coordinate system, shown schematically in the image of experiment C1, is outside of the image. In the images (column I), crests correspond to the white regions and troughs correspond to the dark regions.

nodal region and traverses in x. We note however, that these data do not provide an explanation for the connecting leg seen in the contour maps of the images.

Figures 10(c) and 11(c) show the time-series obtained in the nodal region for experiments C1–C8 (fixed nonlinearity; variable aspect ratio) and for C9–C14 (fixed aspect ratio; variable nonlinearity). The data show a constant water surface displacement in the nodal region for experiments C3–C10 ($a_0\kappa \leqslant 0.20$) indicating that these cells are indeed rectangular. Oscillations in the nodal region (feature 4 in table 6) are present in experiment C2. They are also apparent in experiments C11–C14, for

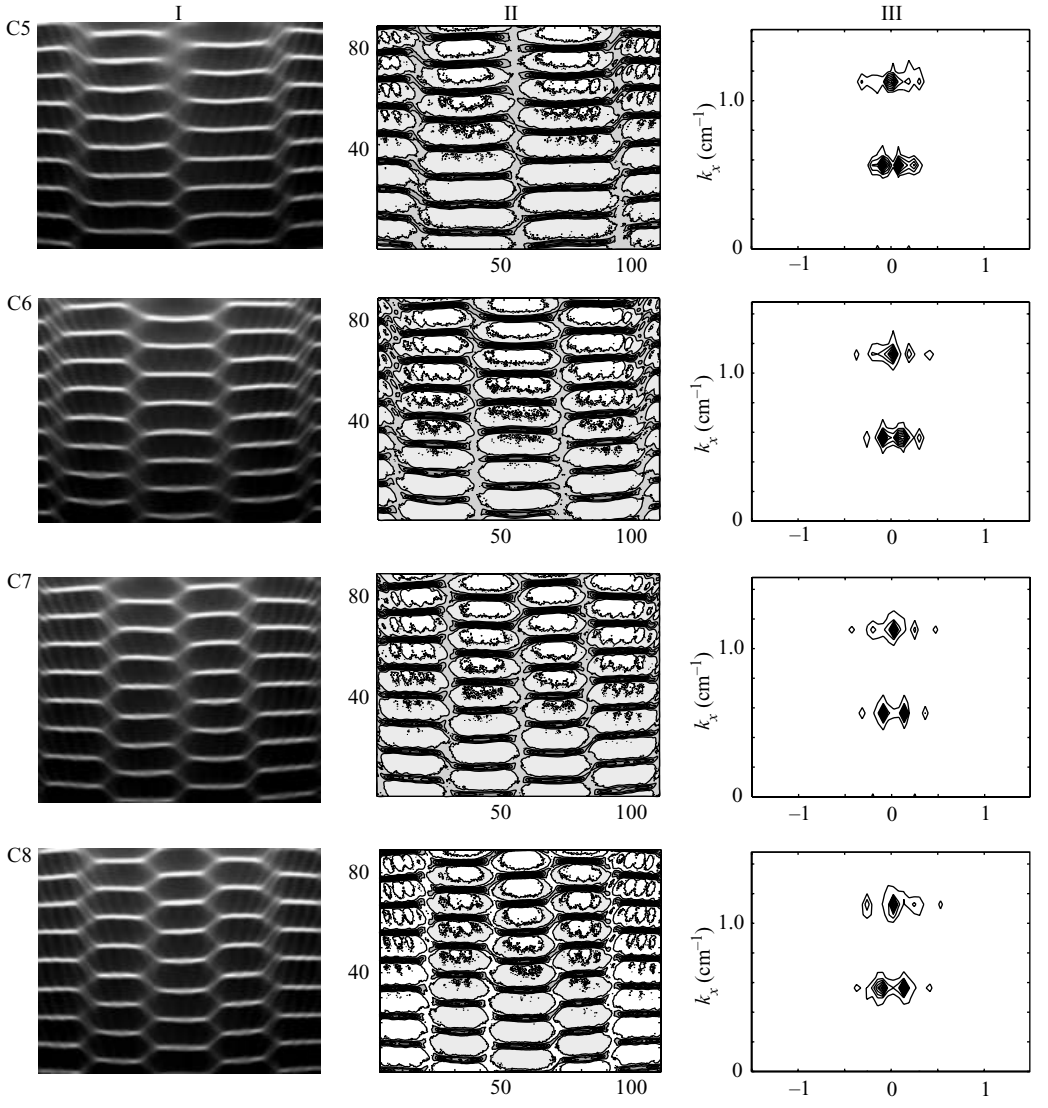

FIGURE 7. As for figure 6, but for $n = 5, 6, 7, 8$. Parameters for experiments C5–C8 are given in table 1.

which nonlinearity is increased over ($0.25 \leqslant a_0\kappa \leqslant 0.40$). Unlike similar oscillations in a hexagonal pattern, which would have multiple frequencies, the oscillations in C2, C11–C14 have the same frequency as the carrier waves. Thus, they are more probably due to a slow evolution of the nodal lines. Their consistent appearance in experiments C11–C14 indicates they are likely to be due to finite nonlinearity. Their appearance in experiment C2 does not fit that argument. A difference between experiment C2 and the other experiments with the same nonlinearity (experiments C1–C8 with $a_0\kappa = 0.20$) is the aspect ratio. C2 had the longest y-wavelength of this set of experiments, except for C1, which was a one-dimensional experiment with no nodal lines. (We discuss this evolution further in § 5.2.)

Further evidence of slow evolution in the wavetanks is shown in figures 10(a, b) and 11(a, b). Figures 10(a) and 11(a) show the time series from a gauge that is positioned

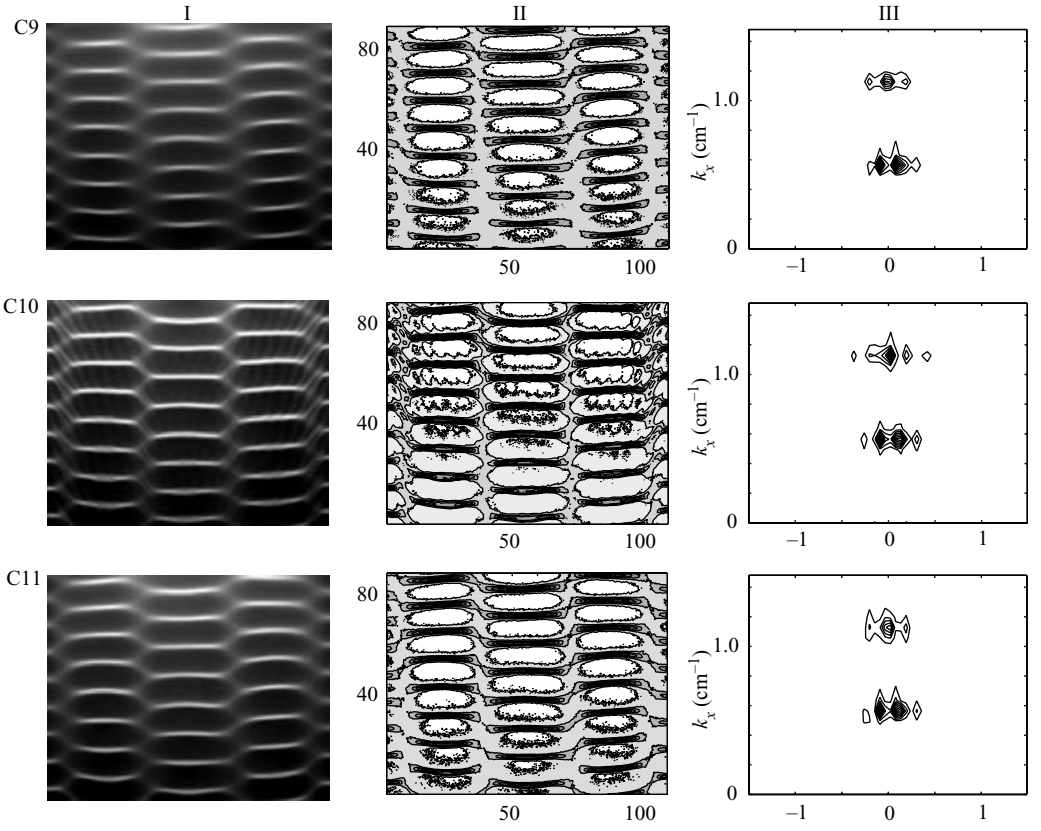

FIGURE 8. Images (column I), contour maps (column II) and spatial Fourier transforms (column III) of 4 Hz waves with $n = 6$ and $a_0\kappa = 0.15$, 0.20 and 0.25. Parameters for experiments C9–C11 are given in table 2. Surface patterns propagate from top to bottom of the image. In the images (column I), crests correspond to the white regions and troughs correspond to the dark regions.

at a fixed y-location in the antinode of the cell pattern and traversed in the x-direction. Figures 10(b) and 11(b) show the Fourier transforms of those time series. The data from experiments C1–C8 (fixed nonlinearity at $a_0\kappa = 0.20$, variable aspect ratio) show primarily viscous decay with nascent modulations (feature 5 in table 6) most visible in experiment C3. The modulations are reminiscent of the Benjamin–Feir (Benjamin & Feir 1967) instability for one-dimensional waves (see § 5.1). Experiment C1 used a one-dimensional wave field; as discussed in (11) in § 5.1, Benjamin–Feir theory predicts that the most unstable sidebands occur at 2.92 and 4.85 Hz. The spectrum (figure 10b) for experiment C1 shows sideband peaks at 3.13 and 4.86 ($\pm$ 0.11) Hz, which are fairly close to the predictions of the most unstable modes. With varying aspect ratio, other sidebands become dominant; in experiments C6, C7 and C8, the sidebands with the most energy are observed at frequencies of 2.16, 2.27 and 2.49 Hz. The data for experiments C9–C14 (fixed aspect ratio with $n = 6$, increasing nonlinearity) show that as nonlinearity is increased, the modulations in the x-direction become much more pronounced. The Fourier transforms (figures 11b) of the time series of these two-dimensional patterns taken in the crest region show that the frequencies of the most unstable sidebands stay close to that of the carrier wave when

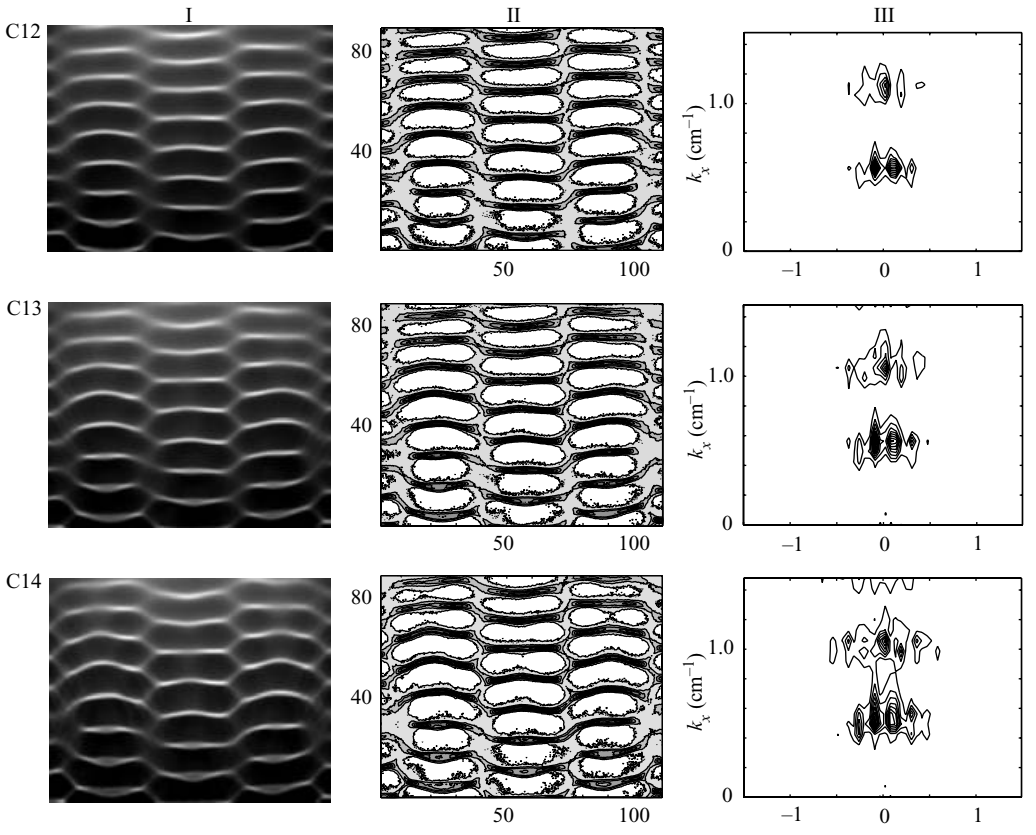

FIGURE 9. As for figure 8, but with $a_0\kappa = 0.30$, 0.35, and 0.40. Parameters for experiments C12–C14 are given in table 2.

the carrier wave nonlinearity is increased. This behaviour is in contrast to results from the one-dimensional theory, for which the frequency of the most unstable mode separates significantly from that of the carrier-wave frequency with increasing carrier-wave amplitude. For example, for experiment C14, the measured dominant sideband is at about 3.5 Hz, while the one-dimensional, Benjamin–Feir theory predicts it to be at about 2.2 Hz.

A feature (6 in table 6) that is not due to slow evolution is also present in both the images and corresponding contour maps of experiments C2–C8 (and C10, which is the same experiment as C6). It is the small-scale periodicity at an angle to the x-axis. It is not visible in the image and contour map for the one-dimensional experiment, C1, or the experiments in which nonlinearity was increased (C9–C14, except C10 = C6). This small-scale wave is especially evident in the nodal lines of the images, and in the crestlines of the contour maps. It had the same periodicity in each experiment.

The small-scale waves should also be apparent in time series of the water surface displacements obtained from a gauge at a fixed x-location that traverses in the y-direction. Figures 12 and 13 show such time series from experiments C1–C8 (fixed nonlinearity; variable aspect ratio) and C9–C14 (fixed aspect ratio, increasing nonlinearity). The data are obtained from two gauges traversed at $x = 50$ cm (figures 12*a* and 13*a*) and $x = 100$ cm (figures 12*b* and 13*b*) from the wave paddle array in the y-direction. The x-wavelengths for experiments C1–C14 are about 10 cm; thus, the x

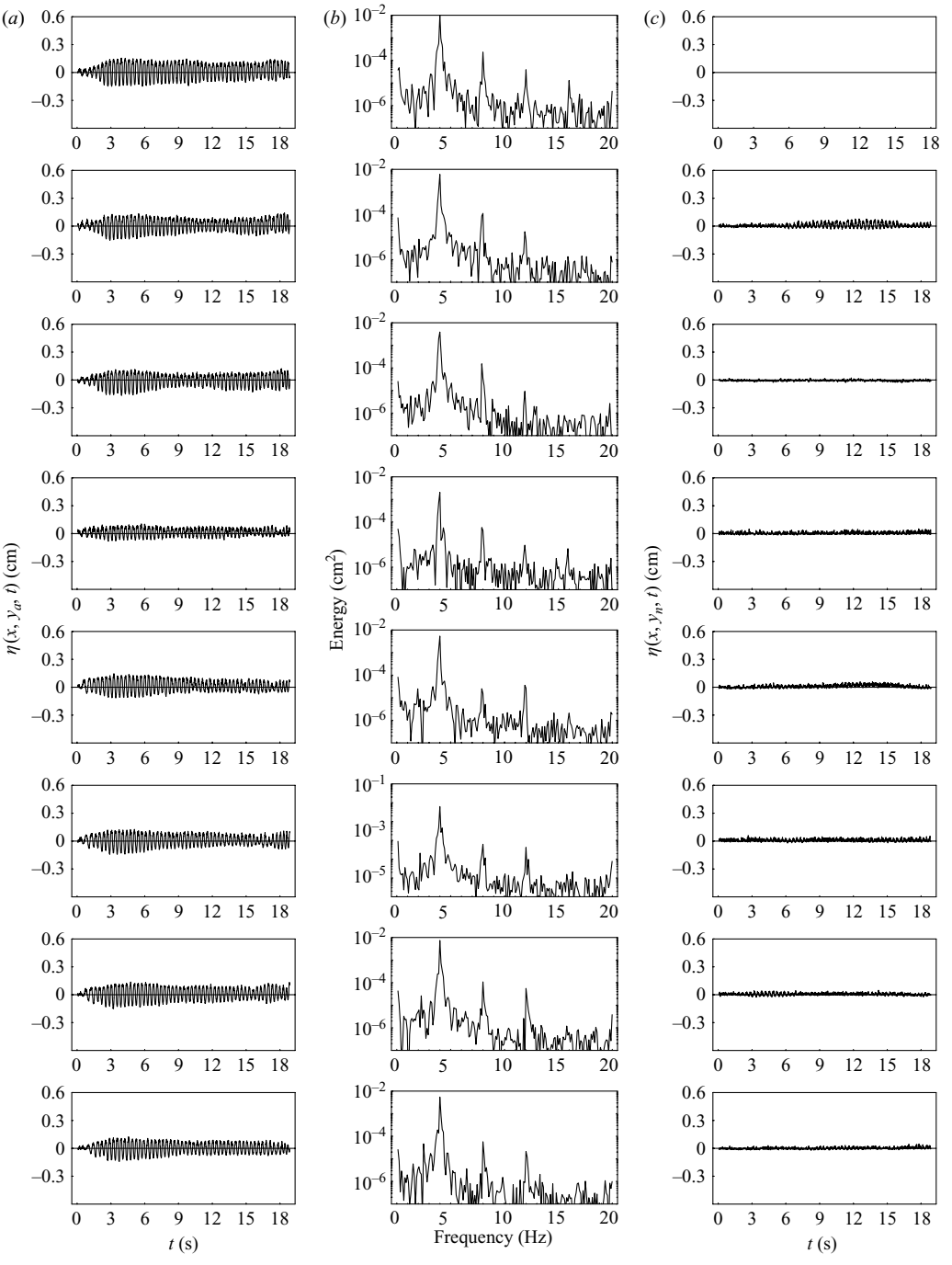

FIGURE 10. Measurements of water surface displacement as a function of time during an x-traverse taken at (a) y_a, an antinodal line with (b) corresponding Fourier transforms and (c) y_n, a nodal line. Rows correspond to experiments C1–C8 in table 1.

distances correspond to about 5 and 10 wavelengths from the wavemaker array. As the gauges traversed, the wave patterns propagated under them in the x-direction; thus, the time series represent a traverse through the spatial pattern at a known angle.

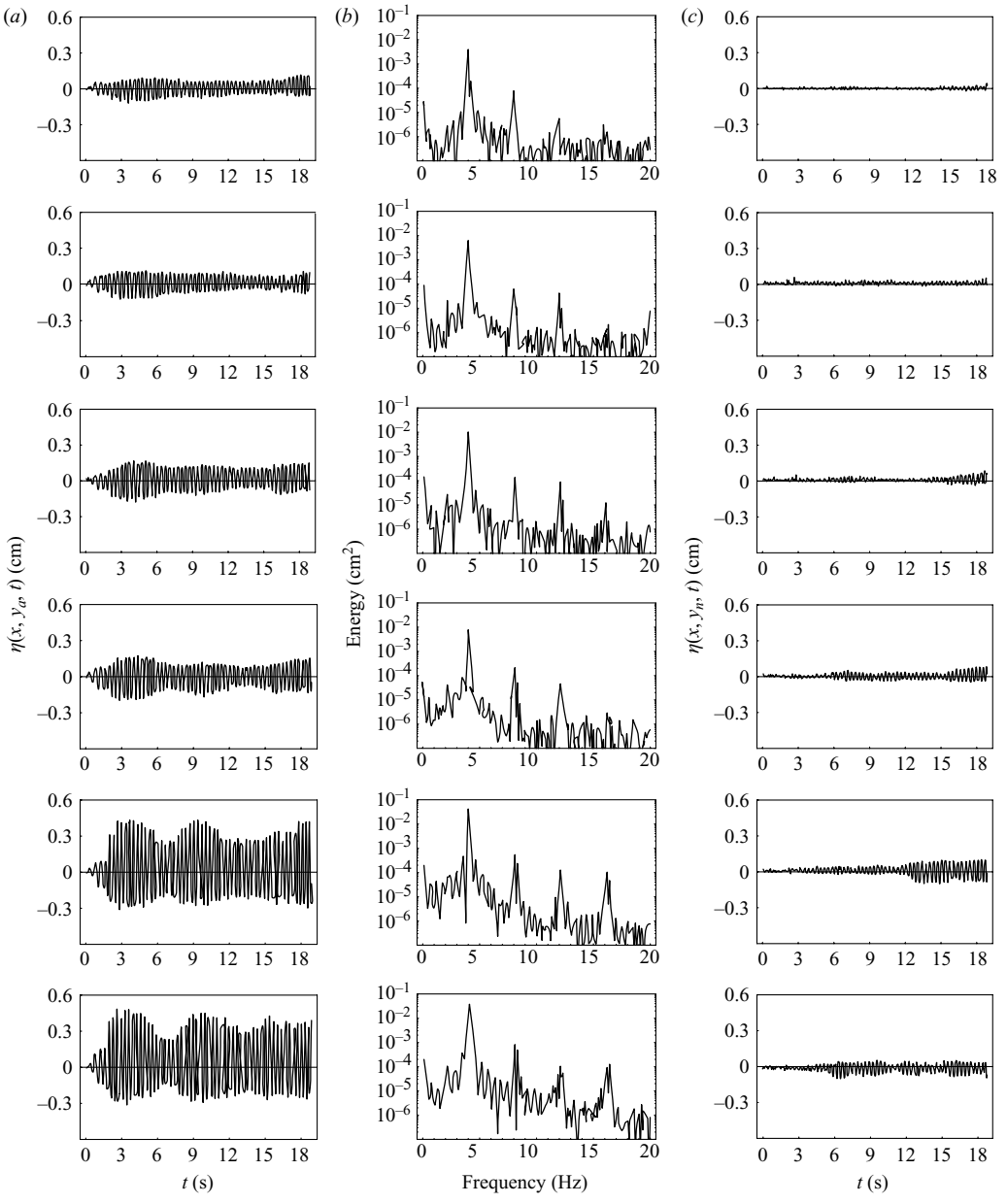

FIGURE 11. As figure 10, but for experiments C9–C14 in table 2.

Faintly visible on the crests of the carrier waves within the larger y-variations of the crestlines is a small jaggedness that could be the manifestation of the small-scale waves in the time series. This jaggedness is hard to see; a particular example occurs on the individual crests of the underlying waves in the time series shown in the fourth row of figure 12(a) (experiment C4). It seems to be present in every experiment except C13 and C14, which have the largest underlying carrier waves. We note that the time series are obtained at x-locations closer to the wavemaker array than the location of the images of the experiments shown in figures 8 and 9. So, the jagged structure is

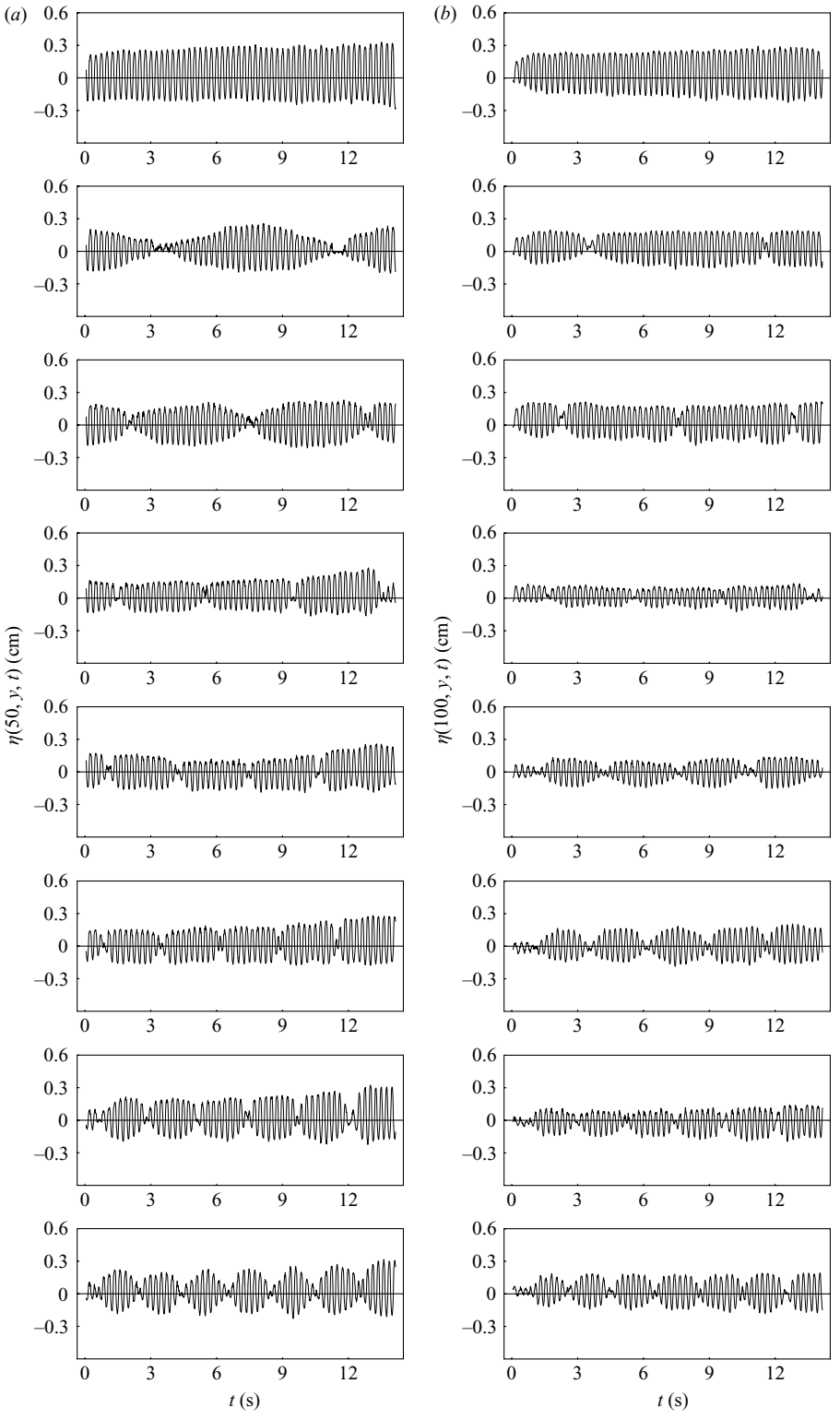

FIGURE 12. Measurements of water surface displacement as a function of time during a y-traverse for (a) $x = 50$ cm and (b) $x = 100$ cm. Each row corresponds to experiments C1–C8 in table 1.

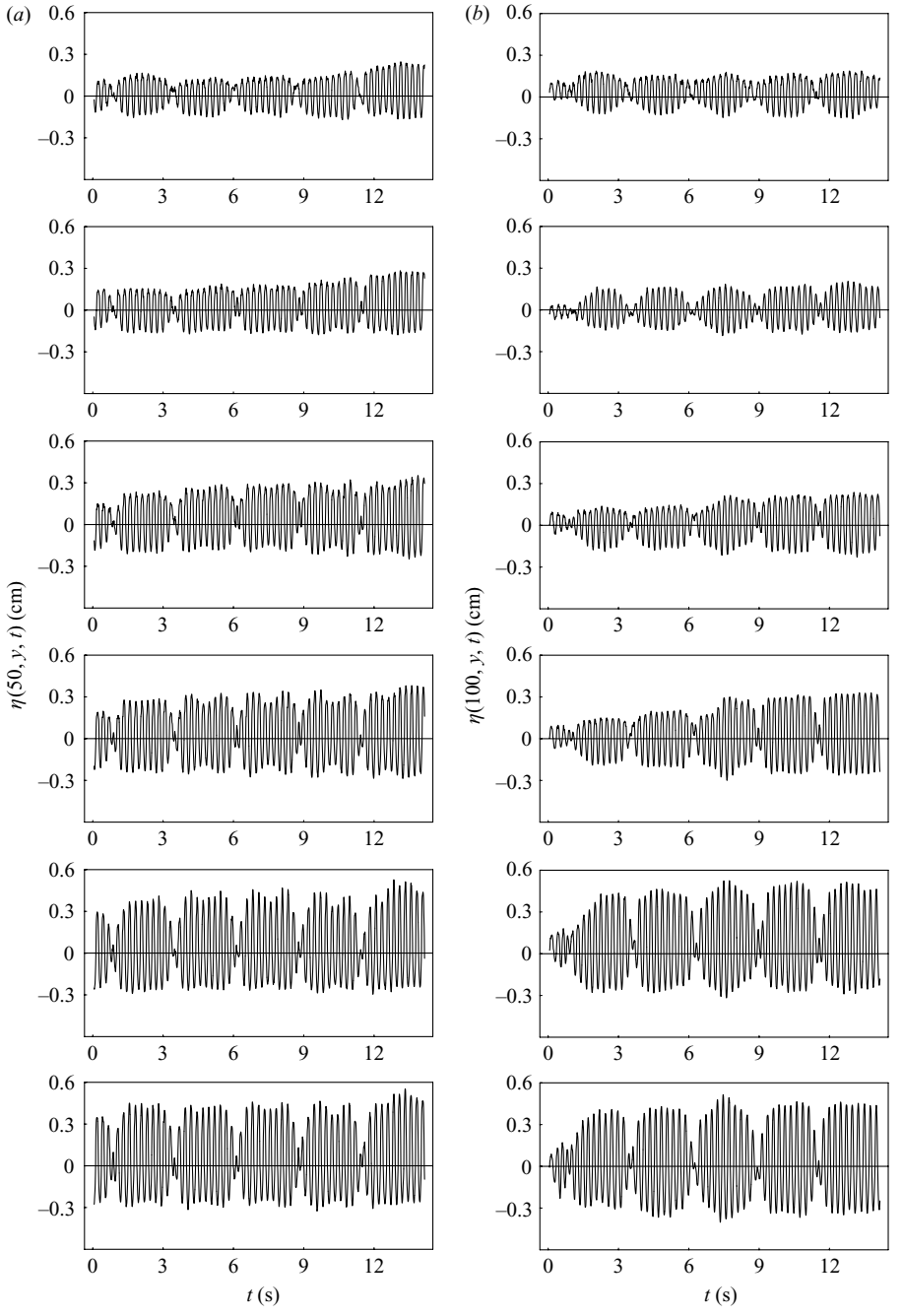

FIGURE 13. As for figure 12, but for experiments C9–C14 of table 2.

present in the time series of experiments C1, C9 and C11, but must have died out before progressing far enough down the tank to appear in the corresponding images.

A transient feature that is apparent in two of the experiments is the 'pinch-off' (feature 7) of cells. The extra structure in these wave fields is apparent in the Fourier transforms of the images, but is most easily seen in the contour maps of the images.

For example, the contour map of the image from experiment C2 shown in figure 6 (column II), shows two cells that appear to have pinched into three separate cells. This effect is transient; it did not persist with increasing x as seen in the image. This experiment was the only one we saw in which the pinch-off was to three cells. More commonly, the cells tended to pinch into two cells. For example, the contour map of the image from experiment C14 shown in figure 9 (column II), shows several cells that appear to have pinched into two separate cells or begun pinching into two cells. The pinching becomes more significant with increasing nonlinearity. For example, consider the contour maps from the increasingly nonlinear experiments, C12, C13 and C14: figure 9 (column II). More specifically, consider the first three rows of the two outside sets of cells in each figure. These cells appear asymmetric in experiment C12 ($a_0\kappa = 0.30$); there is evidence of nascent pinching in experiment C13 ($a_0\kappa = 0.35$); and pinch-off occurred in experiment C14 ($a_0\kappa = 0.40$). One conclusion is that this pinch-off is related to nonlinearity. We provide an explanation consistent with this conclusion in § 5.2.

The pinch-off should also be apparent in time series of the water surface displacements obtained from a gauge at a fixed x-location that traverses in the y-direction. The contour maps of the images indicate that if a pinch-off is present, there should be regions of larger amplitudes on either side of a depressed region along a traverse in the y-direction. We refer to the depressed region as a 'dip' (feature 8 in table 6), and look for it in time series obtained from the y-traverses.

Figure 13 shows the y-time series of wave fields from experiments C9–C14 for which nonlinearity was increased over $0.15 \leqslant a_0\kappa \leqslant 0.40$. The y-time series show that at $x \approx 5$ wavelengths from the wavemaker (figure 13a), the experiments with $a_0\kappa > 0.20$ had a dip in the center of the crest region that became more pronounced with increasing nonlinearity. However, in none of the experiments did the crest regions retain this dip a further 5 wavelengths from the wavemaker. In some of the experiments, the crest regions regained their cosine structure in y, and in some, the crest regions became flat.

Figure 12 shows analogous time series of wave fields from experiments C1–C8 (fixed nonlinearity of $a_0\kappa = 0.20$, variable aspect ratio). These data do not show such a strong appearance of dips, but do show that the crest-regions in the y-direction flattened out, in contrast to the cosine dependence imposed at the wavemaker. This flattening of cosine crest regions is feature 9 in table 6. At $x = 50$ cm from the wavemaker (figure 12a), only experiments C2, C3 and C8 ($n = 2, 3, 8$) retained the cosine structure, but generally flattened out further downstream of the wavemaker. Experiment C2 did develop some modulations on the bottom half of the y-crestline envelope at $x = 100$ cm from the wavemaker (figure 12b); these modulations may (or may not) be consistent with the pinching into three cells that was a transient feature of the image of experiment C2. The crest-regions of experiments C4–C7 ($n = 4$–7) had already flattened out at $x = 50$ cm. Further downstream, the y-crestlines of C4 developed dips, particularly in the bottom half of the crest-envelopes. However, the contour map of the image of experiment C4, taken downstream from the location of this time series, does not show evidence of a corresponding pinch-off region. Further downstream, the y-crestlines of C5–C7 regained, at least partially, their original cosine dependence.

A final manifestation of slow evolution is a time-varying width of the nodal region (feature 10 in table 6) in some of the experiments. It is evident in the contour maps (column II) of experiments C3, C4 (figure 6), C9, and C11 (figure 8). It does not seem to be correlated either with varying aspect ratio or varying nonlinearity. It is possible that the time-varying width of the nodal region is related to the modulations in the x-direction (feature 5). We discuss this possible scenario in § 5.2.

The data taken from experiments C1–C8 in which nonlinearity was held fixed and aspect ratio was varied showed, generally, wave patterns that persisted with slow evolution in the wavetank. In experiments C9–C14, the nonlinearity of the wave fields was increased. Accordingly, the degree of evolution increased. To examine an example of more pronounced evolution, consider figures 14 and 15, which comprise a sequence of images taken from a single experiment, C14 ($a_0\kappa = 0.40$), the most nonlinear experiment. The imager travelled at 10.59 cm s^{-1}, which corresponds to half the energy velocity of the underlying carrier waves. The midpoint of the first image was 80 cm from the wavemaker array. Images were obtained at time increments of 1 s, so that the distance from the wavemaker to the center of the mth image ($m = 1$–10) is $(80 + 10.59(m - 1))$ cm. Each image overlaps the previous one in space such that the bottom 7 rows of cells in one image correspond spatially to the top 7 rows of cells in the subsequent image with a 1 s temporal offset. Figures 14(a) and 14(b) show the images obtained as the imager travelled above the tank in the x-direction along the centreline of the tank. Figures 14(b) and 15(b) show the contour maps obtained from the grey levels of the images, and 14(c) and 15(c) show the Fourier transforms obtained from the grey levels of the images. (We note that figure 15(c) is the same as figure 9, row 3.) Two features already discussed are quite prominent in the sequence of images: (i) feature 7, the pinch-off of the cell into two cells; and (ii) feature 10, the time-varying width of the nodal lines.

Feature 7, the pinching of cells into two cells, appears first, perhaps in figure 15(a) (column II), with a narrowing in the x-direction of the crest region at the top of the contour map. The x-narrowing is enhanced in figure 15(b) (column II) in almost the same location, and pinch-off occured in figure 15(c) (column II). The pinched-off regions separated within the same cell in the next image, where pinch-off events occurred in other downstream cells as well. In the final image, figure 15(e) (column II), there are several regions of pinch-off throughout the pattern.

Feature 10, the time-varying width of the nodal lines, first appeared perhaps in figure 14(c) (column II) in the top part of the contour map and continued further into the top half of figure 14(d) (column II). Here the nodal line was wider at the top of the contour map and narrowed in the positive x-direction to a minimum near the center of the contour map. This orientation changed in the next image, figure 14(e) (column II), where the nodal line widened in the positive x-direction, ending with the development of a very different looking cell in the center. The white crest region in the center was contracted in the y-direction to about 1/3 that of the original cells. In successive images and contour maps (figure 15a–c, column II), this 'contracted cell' moved toward the bottom of the frame. (We note that the image and contour in figure 15(c) are the same as columns I and II in C14 of figure 9.) The contracted cell reached the bottom of the image in figure 15(d) (column II) but a similar region appeared at the top of that frame. This new contracted region then moved down the image in figure 15e (column II).

An additional feature is apparent in C14, the most nonlinear experiment. Downstream from the region of a broadened nodal line region (as in figures 14a–14d, column II) and downstream of a contracted cell (figures 14(e) and 15(a–e), column II) is a region where the crest-regions have broadened (instead of the nodal region), and the nodal region has more of a zigzag structure than a nodal line. In regions with this zigzag structure (feature 11 in table 6), we cannot draw a line that traverses only one contour level. In contrast, a similar zigzag structure can be seen in the contour map for a less nonlinear experiment, like C8; however, we can draw a line down its nodal region and stay in a single contour level. This result is consistent with

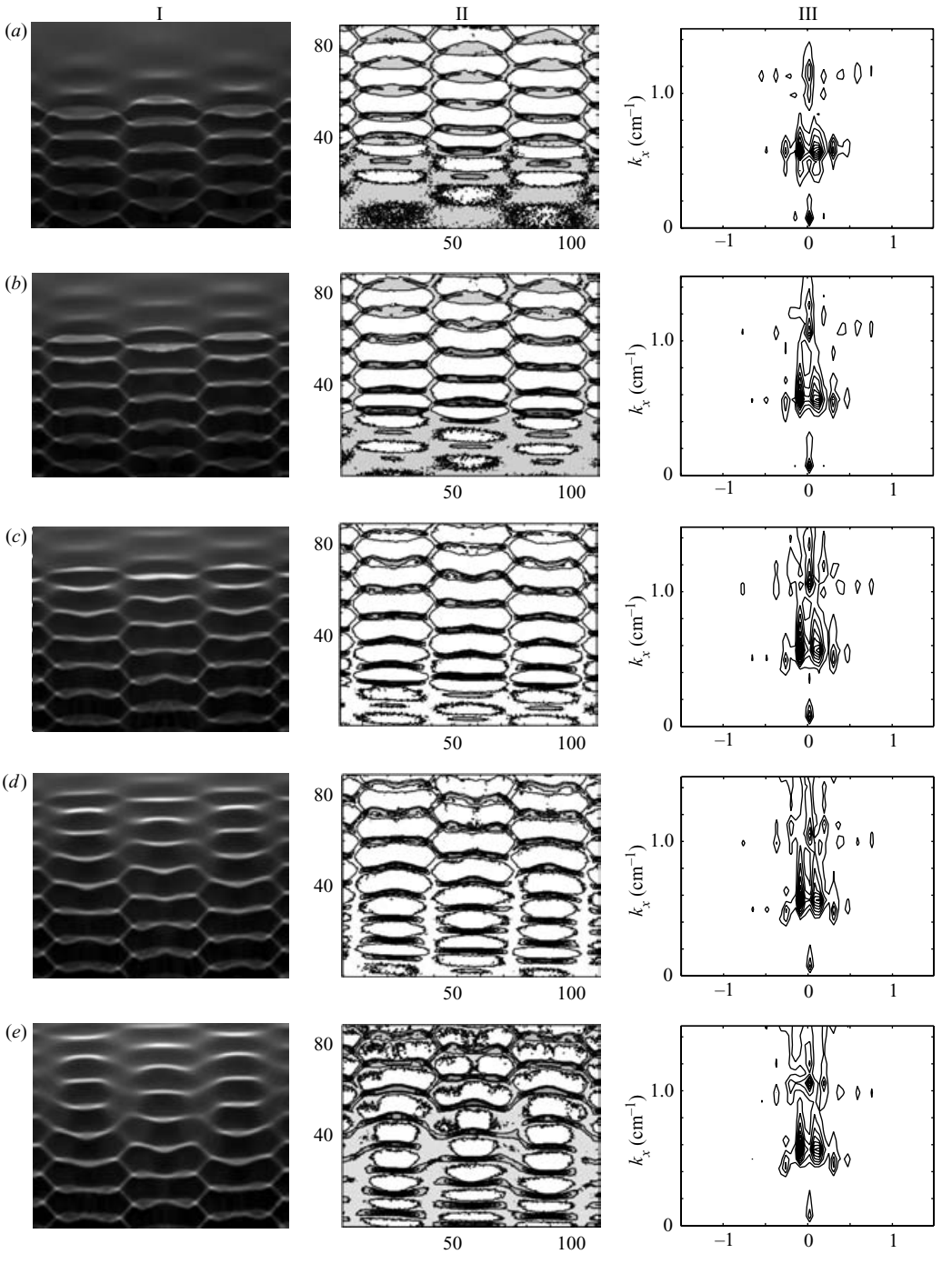

FIGURE 14. Images, contour maps, and Fourier transforms of experiment C14 (4 Hz waves with $a_0\kappa = 0.40$, $n = 6$ and $\rho = 0.33$) as the wavetrain propagates down the tank. The midpoint of the images is $80 + 10.59(m - 1)$ cm from the wavemaker array where (*a*) $m = 1$, (*b*) 2, (*c*) 3, (*d*) 4 and (*e*) 5. Surface patterns propagate from top to bottom of the image. In the images (column I), crests correspond to the white regions and troughs correspond to the dark regions.

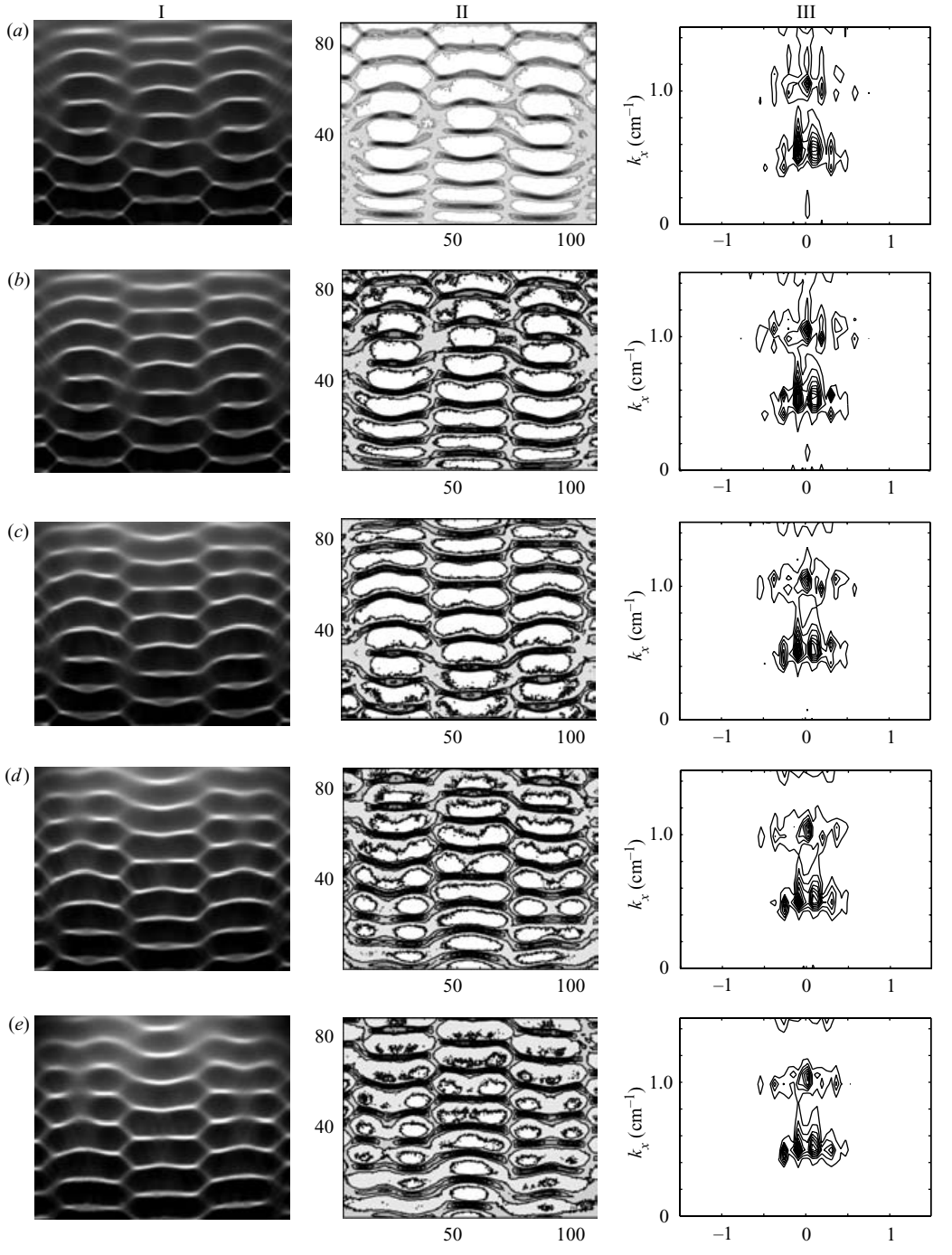

FIGURE 15. As for figure 14, but (*a*) $m = 6$, (*b*) 7, (*c*) 8, (*d*) 9 and (*e*) 10. Row (*c*) is the same as row C14 in figure 9.

time series measurements taken when the gauge traversed through the nodal lines in the x-direction. In experiment C8 (figure 10, row 8), there were no oscillations; in experiment C14 (figure 11, row 6), there were, and these oscillations had an envelope that is qualitatively consistent with the zigzag structure's being present in some parts

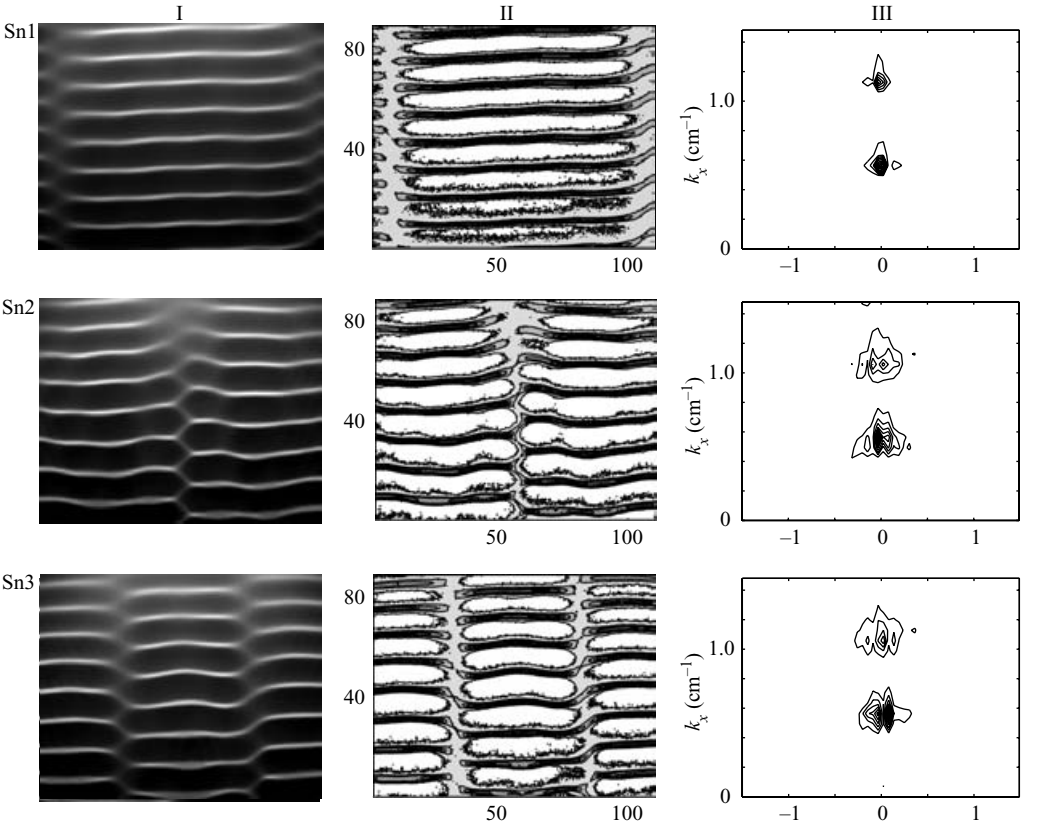

FIGURE 16. Images (column I), contour maps (column II) and spatial Fourier transforms (column III) of experiments Sn1–Sn3 using a Jacobi elliptic sine modulation on the paddle array. The parameters for the experiments are given in table 3. In the images (column I), crests correspond to the white regions and troughs correspond to the dark regions.

of the wave field, but not in all. On the other hand, experiments C12 and C13 also show oscillations in the x-time series (figure 11, rows 4 and 5), we but in the corresponding images (figure 9a, b) we can draw a line down the nodal regions and stay in a single contour level.

Finally, experiment C14 exhibits the last feature we list, 12 in table 6, curvature in the crest lines, parallel to the wavemaker array. The curvature, seen in both the image and the contour maps in the third row of figure 9, is much larger than the distortion caused by the imager lens, shown in figure 2.

4.2. *Experiments with Jacobi elliptic sine envelopes*

The second type of forcing we considered used carrier waves propagating in the x-direction with Jacobi elliptic sine function modulations in the y-direction so that the paddle displacements are described by (2) in § 2. Parameters for six experiments are presented in table 3. Figures 16 and 17 show the images, corresponding contour maps, and corresponding Fourier transforms for the six Sn-experiments. The centers of the images are $x = 154$ cm from the wave paddles as were the analogous images for experiments C1–C14. Figure 18(a) shows the time series obtained when two gauges were traversed in the y-direction at fixed $x = 50$ cm and figure 18(b) shows $x = 100$ cm. Figure 19(a) shows the time series obtained when two gauges were traversed in the

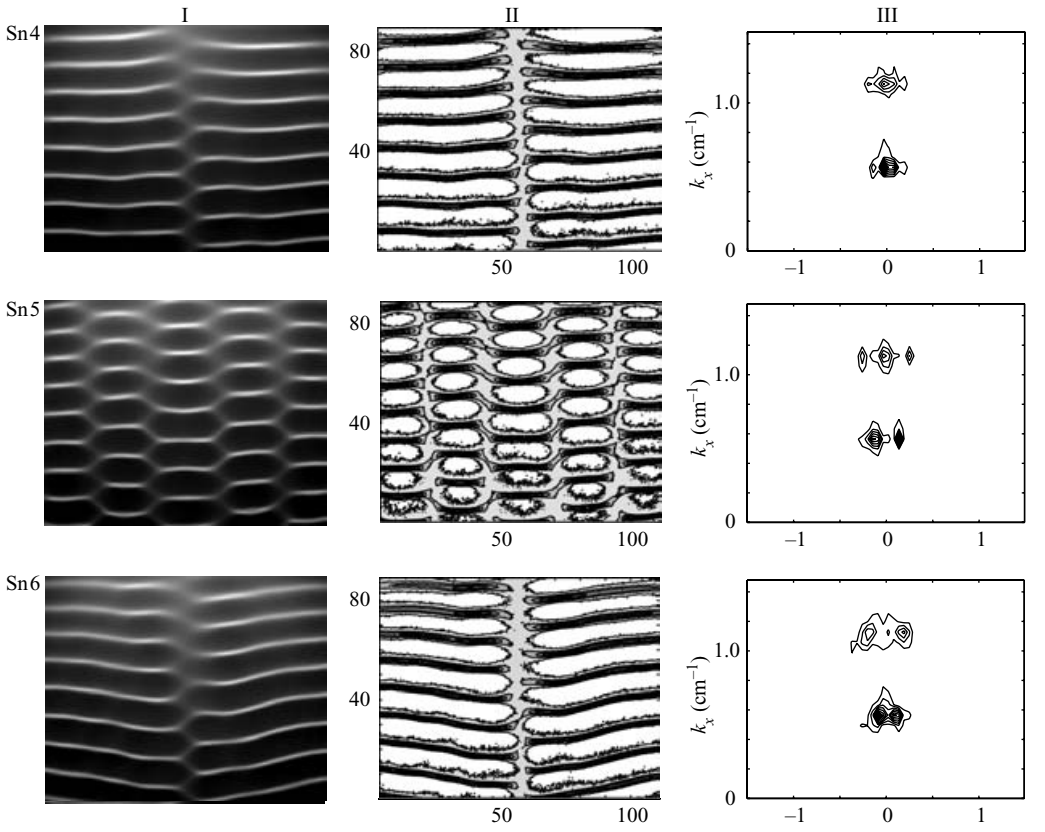

FIGURE 17. As for figure 16, but for experiments Sn4–Sn6.

x-direction at fixed y-values in the crest-region and figure 18(c) in the nodal region. The Fourier transform of the data in figure 19(a) is shown in figure 19(b).

Here we discuss the Sn-experiments within the framework of experimental observations listed in table 6 and defined above with respect to the cosine experiments. The cells in the Sn-experiments exhibit many of the same features, do not exhibit others, and have some of their own.

Feature 1: persistence. The images of the Sn-experiments show that they comprise wave fields with two-dimensional surface patterns that persist with some evolution within the wavetank length. The evolution is described by features 2–12 as discussed below.

Features 2–4: geometry; connecting leg between cells, and oscillations in the nodal region. The contour maps from the Sn-experiments show cell structures that look more like the rectangular cell in the schematic drawing of figure 5 than the hexagonal cell shown there. Nevertheless, the contour maps of all of the experiments except those of Sn4 and Sn6 have connecting legs between some cells. The x-time series (figure 19c) shows that only these two experiments, Sn4 and Sn6, have a genuine nodal line of no surface displacement. The other Sn-experiments have oscillations in the nodal region. Since the experiments with/without connecting legs also did/did not exhibit oscillations in the nodal region, it is likely that these two features are different

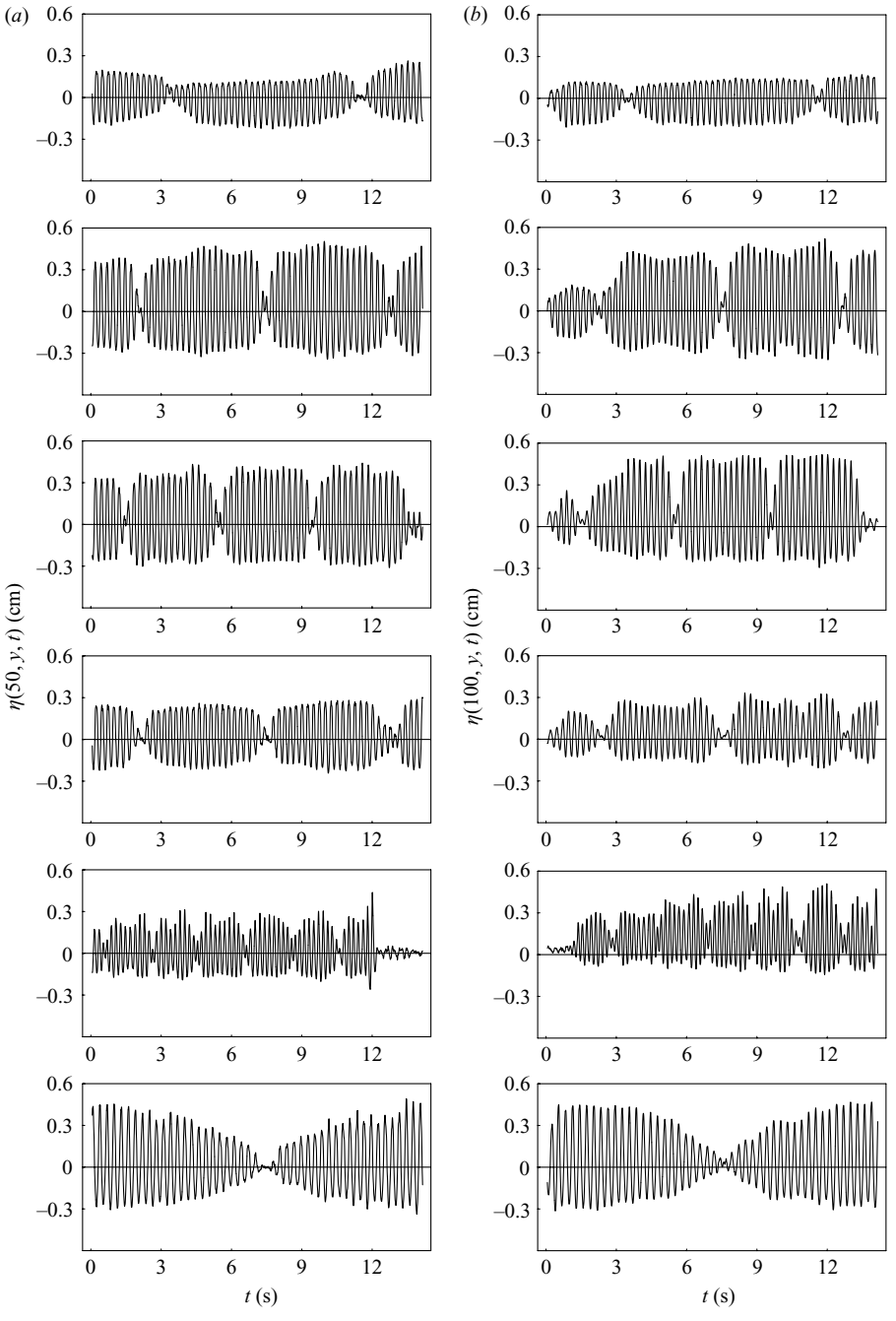

FIGURE 18. Measurements of water surface displacement as a function of time during a y-traverse for (a) $x = 50$ cm and (b) $x = 100$ cm. These experiments correspond to experiments Sn1–Sn6 of table 3.

manifestations of the same structure. We note, however, that the oscillations have the same frequency of the carrier wave, so are not due to a hexagonal cell structure.

Feature 5: modulations in the x-direction. The x-time series (figure 19a) show that all of the experiments exhibit some modulation in the direction of propagation. The

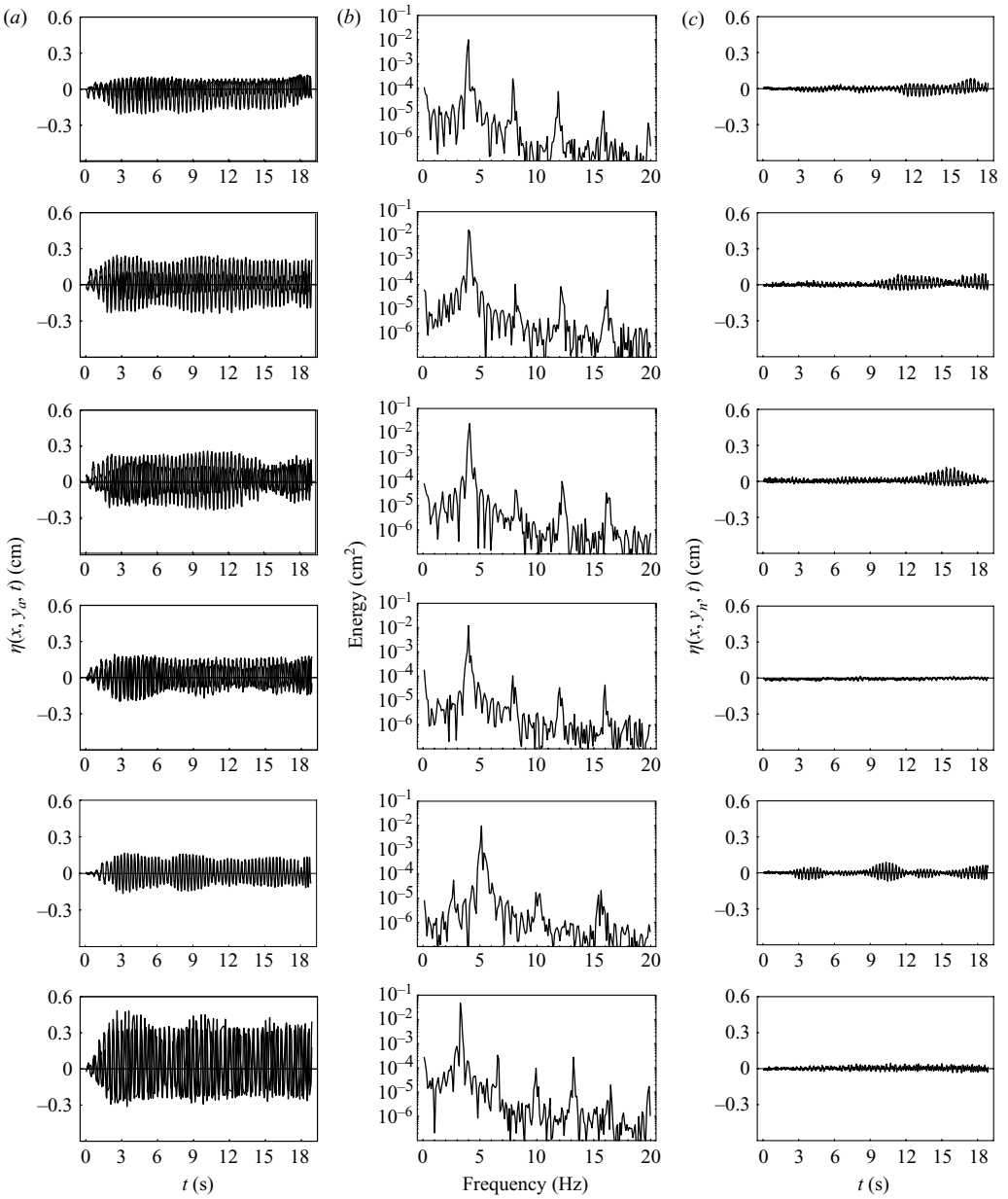

FIGURE 19. Measurements of water surface displacement as a function of time during an x-traverse taken at (a) an antinodal line with (b) corresponding Fourier transforms and (c) a nodal line. These experiments correspond to experiments Sn1–Sn6 of table 3.

Sn-experiments all have large elliptic moduli, m, so that the crest-regions are flat. Therefore, we might wonder if they can be modelled, locally, as a one-dimensional Stokes wavetrain. One consequence of this model is the classic Benjamin–Feir instability (1967), which predicts the most unstable sideband frequencies (11) for a given carrier wave amplitude and frequency. Experiment Sn1 has the smallest nonlinearity ($a_0k = 0.16$). The predictions corresponding to Sn1 are 3.18 Hz and 4.67 Hz; the measurements for Sn1 were at 3.35 Hz and 4.32 ± 0.11 Hz, a difference of about 5

and 7 %. With increasing nonlinearity, the agreement became worse: for experiment Sn6 ($a_0k = 0.18$), the lower sideband disagreed with the Benjamin–Feir prediction by about 12 %, while the upper sideband disagreed by about 2 %. For experiment Sn4 ($a_0k = 0.22$), the lower and upper sidebands disagreed by about 14 %. For experiments Sn2 and Sn3 ($a_0k = 0.32$ for both) disagreement was about 30 %. In experiment Sn5, which has a carrier wave frequency of 5 Hz, the Fourier transform of the time series shows that the most unstable lower sideband is at 2.68 ± 0.12 Hz, which is close to 2.50 Hz, the subharmonic of the carrier wave.

Feature 6: small-scale waves. None of the images and contour maps of the Sn-experiments show the small-scale waves that were evident in the cosine experiments, C2–C8. However, the time series (figure 18) obtained from traversing the gauge in the y-direction do show the jagged structure on the individual crests (as discussed above for the cosine experiments) in experiment Sn1 (see the first row of data in figure 18). The time series from experiment Sn4 shows the jagged structure at $x = 50$ cm from the wave paddles, but not at $x = 100$ cm. We have no explanation as to why they did not appear as ubiquitously as with the cosine experiments. However, we note that experiments Sn2, 3, 5 all have values of nonlinearity ($a_0k = 0.32, 0.32, 0.35$) that are as large as those of experiments C13 and C14 where the small-scale waves also were not visible.

Feature 7, 8: pinch-off of cells; dips in crests. None of the images shown in figures 16 and 17 show pinch-off events; however, the y-time series shown in figure 18 for experiments Sn2–5 show significant dips in the crestlines parallel to the wavemaker array. The time series were not obtained in the same location as the images show; nevertheless, we note that images taken where the time series were taken also do not show pinch-off events.

Feature 9: flattening of crests. The Sn-experiments were chosen with values of elliptic modulus m to ensure that the tank endwalls (perpendicular to the wavemaker array) were lines of symmetry and to obtain y-crestlines that were as flat as possible. So, we put in flat crests at the wavemaker. Figure 18 shows that in some experiments, the crestlines became dipped, and in some instances, the crestlines developed a cosine-like shape, like those of the fourth and fifth groups of the y-traverses shown in figure 18 for experiment Sn5.

Feature 10, 11: time-varying width of the nodal region; zigzag structure. All of the experiments, except perhaps experiment Sn3, showed some time-varying width of the nodal region. It developed in a positive x-direction in experiments Sn1 and Sn5. It developed in a negative x-direction in experiment Sn6 and in experiment Sn2, where the narrowing end leads to a zigzag structure.

Feature 12: curving of the crest lines. The images and contour maps from experiments Sn2, 3, 4 and 6 (figures 16 and 17) show curvature of the y-crestlines. It is particularly pronounced in the long y-wavelengths in experiment Sn6. This curvature is much larger than the distortion caused by the imager lens, shown in figure 2.

5. A theoretical framework and qualitative comparison with experimental results

In the previous section we presented data from twenty sets of experiments in which we generated two-dimensional surface patterns near a wavemaker array. The goal of these experiments was to determine whether these patterns persist, what their main

features are, whether standard models of deep-water waves describe these features, and whether there are parameter regimes in which the patterns are stable. Fourteen of the experiments (C1–14) were generated using an oblique interaction of two symmetric carrier waves, which corresponds to a cosine modulation on the crestline. Six of the experiments (Sn1–Sn6) were generated using a Jacobi elliptic sine function modulation on the y-crestline of a carrier wave. We obtained data from overhead images and from time series of surface displacement from gauges that traversed in the x- or y-directions. We listed twelve qualitative features of the experiments in table 6.

In this section we discuss the features listed in table 6 within the framework of standard types of models for the slow evolution of deep-water wavetrains. We address the question: what features observed in the experiments are described by standard models?

5.1. *Theoretical considerations*

Many authors have developed model equations for wave fields with two-dimensional surface patterns. For example, Roberts (1983), Roberts & Peregrine (1983), Roberts & Schwarz (1983) and Bryant (1985) described deep-water waves with two-dimensional surface patterns with a travelling wave high-order expansion of the classic boundary-value problem for water waves, (4). Kimmoun *et al.* (1999) used this approach to describe their experimental observations that showed rectangular surface patterns. Dias & Hărăgus-Courcelle (2000) review standard model equations (the nonlinear Schrödinger equation and Davey–Stewartson equation) and use a dynamical systems approach to model two-dimensional surface patterns as bifurcations, either from a surface at rest or from a one-dimensional wavetrain.

Here our goal is to model the two-dimensional wave patterns observed in the experiments. When these patterns are stationary, their description is a waveform with two phases. So, we consider two approximate models that have exact solutions that result in waveforms with two phases and that were used to design the experiments herein.

The first model is the standard nonlinear Schrödinger equation for the amplitude of a carrier wave propagating in the x-direction with an envelope that may have (long-wave) modulations in both the x- and y-directions. The second is a generalization of the work of Davey & Stewartson (1974) in which we carried out the classic multiple-time scale approach for the case of two carrier waves propagating at arbitrary angles, on finite depth. This approach results in coupled equations for the evolution of the two carrier waves and of mean flows associated with them, if these mean flows exist. A similar approach was used by Pierce & Knobloch (1994) and Pierce & Wayne (1995) for the case of counter-propagating (one-dimensional) carrier waves with an emphasis on accurately describing mean-flow effects. Here we are particularly concerned with the case of infinite depth, for which the mean flow vanishes. The result is two coupled nonlinear Schrödinger equations. Benney & Newell (1967) wrote down coupled nonlinear Schrödinger equations for an arbitrary number of interacting carrier waves without working out the formulae for the coupling coefficients. The infinite-depth version of our coupled model is a particular case of theirs. Equations similar to ours also arise in one-dimensional optics (e.g. Musslimani & Yang 2001).

We refer to the first model as the sNLS (scalar nonlinear Schrödinger equation described below in § 5.1.1), and the second model as the vNLS (vector nonlinear Schrödinger equation described below in § 5.1.2). One exact solution of sNLS is a Jacobi elliptic sine function with a wavelength in the y-direction and no variation in the x-direction. This solution has one phase. The second phase required for a two-phase wave comes from the carrier wave. So, this solution to sNLS, when combined

with the underlying carrier wave using (7*a*), provides a description for the water-surface that corresponds to (2). The resulting pattern is rectangular, with the x-length given by the carrier wavelength and the y-length given by the envelope modulation in that direction.

As we will show in § 5.1.2, there is a family of simple exact solutions of vNLS in which the two complex wave amplitudes each have no spatial dependence, so they each depend only on time. Then vNLS reduces to a coupled set of ordinary differential equations. Solutions in this family correspond to the case of two spatially uniform carrier waves, each one-dimensional, interacting obliquely with each other. When these waves are uncoupled, each is a solution to sNLS, and is commonly called a 'Stokes wave'. When they are coupled through vNLS, the oblique interaction corresponds to a solution for a two-phase wave.

For a special subset of this family, the two underlying (one-dimensional) carrier waves each have the same frequency and the same amplitude, and we orient the coordinate system so that the two wavetrains propagate at equal and opposite angles to the x-axis. Then several pairs of coefficients in vNLS become identical. We call this special case a 'symmetric two-phase wave'.

Symmetric two-phase solutions from vNLS provide a second description for the water-surface comprising a rectangular cell pattern. In this description, the x-length is given by the (same) carrier wavelengths and the y-length is given by the resulting linear wave solution of the two wavetrains propagating at an angle, corresponding to (1). One solution of this form corresponds to the experiment shown in figure 1. The sNLS is applicable for rectangular cells that have a y-length much longer than the x-length. The vNLS is applicable for cells with any aspect ratio. The two exact solutions we consider are equal only in the degenerate limit of zero amplitude.

We derive the evolution equations using the method of multiple scales, which is reviewed, for example, by Dias & Kharif (1999). For both models we begin with the classic boundary-value problem for water waves on an inviscid fluid of infinite horizontal extent and quiescent depth, h, under the influence of a constant gravitational force as formulated by Stokes (1847). We neglect surface tension as a restoring force, based on the smallness of the Bond number for these experiments. The problem formulation for the irrotational velocity field $\boldsymbol{v}(x, y, z, t) = \nabla\phi(x, y, z, t)$ and the free surface displacement $\eta(x, y, t)$ is given by:

$$\Delta\phi = 0 \quad \text{in} \quad -h < z < \eta(x, y, t), \quad -\infty < x, y < \infty, \tag{4a}$$

$$\frac{\partial\eta}{\partial t} + \nabla\phi \cdot \nabla\eta - \frac{\partial\phi}{\partial z} = 0 \quad \text{on } z = \eta(x, y, t), \tag{4b}$$

$$\frac{\partial\phi}{\partial t} + \tfrac{1}{2}|\nabla\phi|^2 + g\eta = 0 \quad \text{on } z = \eta(x, y, t), \tag{4c}$$

$$\frac{\partial\phi}{\partial z} = 0 \quad \text{on } z = -h, \tag{4d}$$

where g is the acceleration due to gravity.

We expand the free-surface displacement and velocity potential in a small paramter, ϵ, such that

$$\eta(x, y, t) = \sum_{j=1}^{\infty} \epsilon^j \eta_j(x, y, t, X_1, Y_1, T_1, T_2), \tag{5a}$$

$$\phi(x, y, t) = \sum_{j=1}^{\infty} \epsilon^j \phi_j(x, y, t, X_1, Y_1, T_1, T_2), \tag{5b}$$

and the variables are functions of slow time and space scales,

$$X_1 = \epsilon x, \quad Y_1 = \epsilon y, \quad T_1 = \epsilon t, \quad T_2 = \epsilon^2 t. \tag{6}$$

Following the standard procedure, we use (5) in (4) and obtain an ordered sequence of inhomogeneous linear boundary-value problems for η_j and ϕ_j. We choose the appropriate first-order solution to derive either sNLS or vNLS and, along the way, solve for $\eta_1, \eta_2, \eta_3, \phi_1, \phi_2$ and ϕ_3.

5.1.1. *sNLS*

Following Ablowitz & Segur (1977), consider a first-order solution corresponding to a monochromatic carrier wave propagating mainly in the x-direction, such that

$$\eta_1(x, y, t) = \frac{\mathrm{i}\omega}{g}(A\mathrm{e}^{\mathrm{i}\theta} - A^*\mathrm{e}^{-\mathrm{i}\theta}), \tag{7a}$$

$$\phi_1 = \Phi_1 + \frac{\cosh\kappa(z+h)}{\cosh(\kappa h)}(A\mathrm{e}^{\mathrm{i}\theta} + A^*\mathrm{e}^{-\mathrm{i}\theta}), \tag{7b}$$

where

$$\theta(x, y, t) = kx + ly - \omega t, \quad \omega^2 = (g\kappa)\tanh\kappa h, \tag{7c}$$

$\omega > 0$ is the frequency, $\boldsymbol{\kappa} = (k, l)$ is the wavevector of a carrier wave that propagates primarily in one direction, with $l = O(\epsilon k)$, $\kappa = \sqrt{(k^2 + l^2)}$, $A(X_1, Y_1, T_1, T_2)$ is the wave amplitude, $A^*(X_1, Y_1, T_1, T_2)$ is its complex conjugate, and $\Phi_1(X_1, Y_1, T_1, T_2)$ represents the mean flow. The amplitude is an envelope that evolves on the slow scales in (6) in a reference frame travelling with the group velocity $\boldsymbol{V} = (\mathrm{d}\omega/\mathrm{d}\kappa, 0)$ evaluated at $l = 0$, which is the linearized group velocity in the limit $l \to 0$.

The envelope is governed by the coupled system of amplitude and mean flow equations derived by Davey & Stewartson (1974), Djordjevic & Redekopp (1977) and others. In the limit of infinite depth, the mean flow vanishes and the envelope, A, of the carrier wave varies according to the sNLS

$$\mathrm{i}\frac{\partial A}{\partial T_2} + \alpha\frac{\partial^2 A}{\partial \tilde{X}^2} + \beta\frac{\partial^2 A}{\partial {Y_1}^2} + \xi|A^2|A = 0, \tag{8}$$

where the coefficients are given in the Appendix and $\tilde{X} = X_1 - |V|T_1$. For gravity-induced waves in deep water, $\alpha < 0$, $\beta > 0$ and $\xi < 0$. The Stokes wave solution is

$$A = A_0\mathrm{e}^{\mathrm{i}rT_2}, \tag{9}$$

with a constant envelope and a frequency correction, $r = \xi|A_0|^2$. Zakharov (1968) showed that this solution is linearly unstable within (8) (for the case of $\beta = 0$) to modes varying in the x-direction when $\alpha\xi > 0$. The mode with the most unstable growth rate has a wavenumber (referenced to $\tilde{X}$), p_m, and growth rate (referenced to T_2), Ω_m, given by

$$p_m = |A_0|\sqrt{\frac{\xi}{\alpha}}, \qquad \Omega_m = \xi|A_0|^2. \tag{10}$$

For comparison with experimental results herein, we choose $\epsilon|A_0| = (a_0 g/\omega)/2$, where a_0 is the amplitude of the carrier wave. Then the prediction for frequency of the most unstable upper and lower sidebands, ω_l^u, relative to the carrier wave frequency, ω, is

$$\omega_l^u = \omega \pm \sqrt{g p_m}. \tag{11}$$

This instability is referred to as the 'Benjamin–Feir' instability after Benjamin & Feir (1967) who computed (11) without using the sNLS equation.

For our application we seek a travelling-wave solution that corresponds to two-dimensional surface patterns. Here, $\beta\xi < 0$, so such a solution to (8) is

$$A = A_0 m \,\mathrm{sn}(cY_1, m)\mathrm{e}^{i\omega_s T_2}, \tag{12}$$

where sn is the Jacobi elliptic sine function, the y-wavenumber is

$$c = |A_0|\sqrt{\frac{-\xi}{2\beta}}, \tag{13}$$

and the frequency correction is

$$\omega_s = \tfrac{1}{2}\xi |A_0|^2(1 + m^2). \tag{14}$$

We note that in general, the elliptic modulus, m, varies over $0 \leqslant m \leqslant 1$, with $m = 0$ corresponding to a sine function and $m = 1$ corresponding to a limiting hyperbolic tangent profile. The corresponding first-order in ϵ expression for the dimensional free surface displacement is

$$\eta = a_0 \mathrm{sn}(cy, m)\sin[kx - (\omega - \omega_s)t], \tag{15}$$

where $|A_0|$ is determined by a given carrier wave amplitude a_0 to be

$$\epsilon |A_0| m = \tfrac{1}{2} a_0 \frac{g}{\omega}. \tag{16}$$

We use (15) to programme the wavemaker in the 'Sn' set of experiments as described in § 2. The corrections due to η_2 and η_3 are required for comparison with experimental results and are given in Appendix A.

5.1.2. *vNLS*

Another approach, which does not assume that the y-variations are long compared to the x-scale of the carrier wave, is to consider a first-order in ϵ solution corresponding to the sum of two carrier waves at arbitrary angles, such that

$$\eta_1(x, y, t) = \sum_{j=1}^{2} \frac{\mathrm{i}\omega_j}{g}\left(A_j \mathrm{e}^{\mathrm{i}\theta_j} - A_j^* \mathrm{e}^{-\mathrm{i}\theta_j}\right), \tag{17a}$$

$$\phi_1 = \sum_{j=1}^{2}\left(\Phi_{1j} + \frac{\cosh\kappa_j(z+h)}{\cosh(\kappa_j h)}\left(A_j \mathrm{e}^{\mathrm{i}\theta_j} + A_j^* \mathrm{e}^{-\mathrm{i}\theta_j}\right)\right), \tag{17b}$$

where

$$\theta_j(x, y, t) = k_j x + l_j y - \omega_j t, \qquad \omega_j^2 = (g\kappa_j)\sigma_j, \tag{17c}$$

the wavevector of the jth wave is $\boldsymbol{\kappa}_j = (k_j, l_j)$ with magnitude $\kappa = \sqrt{k_j^2 + l_j^2}$, and the frequency of the jth wave is $\omega_j = \sqrt{g\kappa_j\sigma_j} > 0$, using $\sigma_j = \tanh\kappa_j h$. The complex amplitude of the jth wave, $A_j(X_1, Y_1, T_1)$, its complex conjugate, $A_j^*(X_1, Y_1, T_1)$, and the meanflow, $\Phi_{1j}(X_1, Y_1, T_1, T_2)$, are functions of the slow scales defined in (6).

At second order we find the usual linear transport equation

$$\frac{\partial A_j}{\partial T_1} + \boldsymbol{V}_j \cdot \nabla_1 A_j = O(\epsilon), \tag{18}$$

for the jth wave, where ∇_1 represents derivatives with respect to the slow spatial scales, and $\boldsymbol{V}_j = (V_{xj}, V_{yj}) = (\partial\omega_j/\partial k_j, \partial\omega_j/\partial l_j)$ is the linear group velocity of the jth wave.

The derivation of sNLS, (8), uses the $j=1$ version of (18) to make a Galilean transformation in the direction of propagation so that the nonlinear Schrödinger equation derived at third order in ϵ is with respect to a reference frame travelling at the linear group velocity of the carrier wave and is independent of ϵ. Here we cannot make such a transformation because the envelopes of the two interacting carrier waves travel in arbitrary directions. Nevertheless, we use (18) to replace derivatives with respect to T_1 by derivatives with respect to (X_1, Y_1) (plus $O(\epsilon)$) in the equations obtained at third order in ϵ. The resulting equations still contain ϵ explicitly, but the replacement shows the connection of the new equations with the familiar Davey–Stewartson equations (1974). They are given by

$$\mathrm{i}\left(\frac{\partial A_j}{\partial T_1}+\boldsymbol{V}_j\cdot\nabla_1 A_j\right)+\epsilon\left(\alpha_j\frac{\partial^2 A_j}{\partial X_1^2}+\beta_j\frac{\partial^2 A_j}{\partial Y_1^2}+\gamma_j\frac{\partial^2 A_j}{\partial X_1\partial Y_1}+\xi_j|A_j|^2A_j+\zeta_j|A_{j+1}|^2A_j\right)=\epsilon(\boldsymbol{\chi}_j\cdot\nabla_1\Phi_{1j})A_j, \quad (19)$$

$$\frac{\partial^2\Phi_{1j}}{\partial T_1^2}-gh\left(\frac{\partial^2\Phi_{1j}}{\partial X_1^2}+\frac{\partial^2\Phi_{1j}}{\partial Y_1^2}\right)=\left(\left[2\omega_j\boldsymbol{\kappa}_j+\kappa_j^2\left(1-\sigma_j^2\right)\boldsymbol{V}_j\right]\cdot\nabla_1|A_j|^2\right), \quad (20)$$

for the envelope of the jth wave and its corresponding mean flow, modulo 2.

The coefficients in front of the linear terms are the same as those in the sNLS for the evolution of the envelope of a single carrier wave. These coefficients correspond to the second derivatives of the frequency of the carrier wave with respect to wavenumbers (Benney & Newell 1967) so that

$$\alpha_j=\frac{1}{2}\frac{\partial^2\omega_j}{\partial k_j^2},\quad \beta_j=\frac{1}{2}\frac{\partial^2\omega_j}{\partial l_j^2},\quad \gamma_j=\frac{\partial^2\omega_j}{\partial k_j\partial l_j}. \quad (21)$$

For the case of one carrier wave, a consequence of choosing the primary direction of propagation (requiring $l=O(\epsilon k)$) is that the cross-derivative term, $\partial^2 A_j/\partial X_1\partial Y_1$, disappears. Here, however, there is no coordinate system that removes this term, except in special cases.

The coefficients in front of the self-interaction term, ξ_j, and in front of the term coupling the wave amplitude and the mean flow, $\boldsymbol{\chi}_j$, are the same as those derived for the analogous term in the sNLS for a single carrier wave (except for scaling differences with classical results, since here the variables are dimensional). The new coefficient, ζ_j, measures the strength of the interaction between the two waves. All of the coefficients are given explicity in Appendix A.

For waves on water of infinite depth, for which $h\to\infty$, the mean flow vanishes, and the equations for the envelopes of the jth waves, modulo 2, become coupled nonlinear Schrödinger equations:

$$\mathrm{i}\left(\frac{\partial A_j}{\partial T_1}+\boldsymbol{V}_j\cdot\nabla_1 A_j\right)+\epsilon\left(\alpha_j\frac{\partial^2 A_j}{\partial X_1^2}+\beta_j\frac{\partial^2 A_j}{\partial Y_1^2}+\gamma_j\frac{\partial^2 A_j}{\partial X_1\partial Y_1}+\xi_j|A_j|^2A_j+\zeta_j|A_{j+1}|^2A_j\right)=0. \quad (22)$$

For symmetric waves propagating on water of infinite depth, the coefficients can be simplified significantly. By 'symmetric waves', we mean two waves for which $k_1=k_2\equiv k$, $l_1=-l_2\equiv l$, $\kappa_1=\kappa_2\equiv\kappa=\sqrt{k^2+l^2}$, $\omega_1=\omega_2\equiv\omega=\sqrt{g\kappa}$, and

$(V_{x1}, V_{y1}) = (V_{x2}, -V_{y2}) = ((g/2\omega)(k/\kappa),\ (g/2\omega)(l/\kappa))$. It follows that for this case,

$$\alpha_1 = \alpha_2 \equiv \alpha = \frac{\omega}{8}\frac{(2l^2 - k^2)}{\kappa^4}, \quad \beta_1 = \beta_2 \equiv \beta = \frac{\omega}{8}\frac{(2k^2 - l^2)}{\kappa^4}, \quad \gamma_1 = -\gamma_2 \equiv \gamma = -\frac{3\omega}{4}\frac{lk}{\kappa^4}, \quad (23)$$

and the coupling coefficients reduce to

$$\xi_1 = \xi_2 \equiv \xi = -2\frac{\kappa^4}{\omega}, \quad \zeta_1 = \zeta_2 \equiv \zeta = \frac{4}{\omega}\frac{(-k^5 + 3k^3l^2 + 5kl^4 + 2k^4\kappa - 2k^2l^2\kappa - 2l^4\kappa)}{k - 2\kappa}. \quad (24)$$

Symmetric two-phase waves, the simplest non-trivial solution to (22) for two symmetric waves, corresponds to the Stokes solution of the nonlinear Schrödinger equation and is given by

$$A_1 = A_2 = A_0\, e^{i\omega_v \epsilon T_1}, \quad (25)$$

where $\omega_v = (\xi + \zeta)|A_0|^2$ is the frequency correction that takes into account the waves' self- and cross-interactions. When (25) is substituted into the first-order solution (17*a*), the expression for the water surface displacement to first order is

$$\eta = a_0 \cos(ly)\cos[kx - (\omega - \omega_v)t], \quad (26)$$

where $a_0 = 4\epsilon|A_0|\omega/g$. We use (26) to programme the wavemaker in the 'C' set of experiments as described in § 2. The corrections for η_2 and η_3 are required for comparison with experimental results and are given in Appendix A.

5.2. *Qualitative comparison of experimental results with sNLS and vNLS*

To compare the experimental results with the Jacobi elliptic sine function solution of sNLS and/or the symmetric two-phase waves solution of vNLS, we use the following procedure based on the theoretical development of § 5.1:

1. Begin with (4).
2. Use asymptotic expansions (5) of the free surface and velocity potential.
3. Substitute them into (4) and carry out the ordered problems to $O(\epsilon^3)$.
4. Obtain expressions for η_1, η_2, η_3, the ordered surface displacements. These expressions are in terms of the carrier wave envelopes and their derivatives with respect to slow scales.
5. At third order obtain the evolution equations:
   (*a*) sNLS (8) for the envelope of a single carrier wave, $A(\tilde{X}, Y_1, T_2)$, corresponding to (2), or
   (*b*) vNLS (22) for the envelopes, $A_1(X_1, Y_1, T_1)$ and $A_2(X_1, Y_1, T_1)$, of two interacting carrier waves, corresponding to (1).
6. Choose an exact, travelling-wave solution of the evolution equation:
   (*a*) the Jacobi elliptic sine function solution (12) of sNLS for the case of a single carrier wave. This solution corresponds to the 'Sn' experiments.
   (*b*) the symmetric two-phase wave solution (25) of vNLS for the case of two symmetric carrier waves interacting at an oblique angle. This solution corresponds to the 'C' experiments.
7. Substitute the exact solutions and their derivatives into the expressions for η_1, η_2, η_3, and construct an expression for the water surface displacement: $\eta = \epsilon\eta_1 + \epsilon^2\eta_2 + \epsilon^3\eta_3$ to third order based on an exact solution of the evolution equation.
8. Use the experiments to choose parameters for input into the solutions for comparison with experiments.
9. Use this third-order solution to construct contour maps of the water surface displacement at a fixed time, and time series of water-surface displacement at a fixed x, while y is varied at a constant speed.

10. Compare with the analogous picture and time series from the experiment.

In making this comparison between theoretical solutions and the experiments, we keep in mind the following:

(i) The hope is that this theory will be able to explain qualitatively some of the features observed in the experiments.

(ii) The theoretical solution represents a travelling wave. Thus, it cannot, by itself, explain the unsteady evolution that is apparent in most of the experiments.

(iii) We can use the parameters of the experiment (amplitude and aspect ratio) to find corresponding theoretical solutions using both sNLS and vNLS.

(iv) The sNLS is valid when the y-wavelength is long compared to the x-wavelength. (Recall that the y-wavelength is twice the cell width.)

(v) The vNLS is valid with no restrictions on aspect ratio.

(vi) The values of a_0 listed for the experiments in tables 1, 2 and 3 were not measured. They were obtained using results from the (experimental) wavemaker problem in one-dimensional as described in § 2.

(vii) The experiments conducted using the Sn-experiments used parameter values (given in table 3) that did not precisely correspond to exact solutions of sNLS, which requires (13)–(16) to be satisfied. This difference was an error and the result is that the experiments introduce a perturbation into the wave fields *ab initio*. The values of exact solutions closest to the experimental parameters are given in table 7 in Appendix B. A comparison of the difference between forcing amplitudes given by the closest exact solution and those used in the experiments is shown in figure 24 in Appendix B for each of the 32 paddles in the six experiments.

(viii) Carter (2001), Carter & Segur (2003) and Aleshkevich *et al.* (2003) have shown that the elliptic function solutions of sNLS and the sn-solution in particular are linearly unstable.

(ix) Similarly, W. Craig, D. P. Nicholls, H. Segur & C. Sulem (personal communication) showed that the symmetric two-phase wave solution of vNLS is linearly unstable.

(x) Despite these instabilities in the (dissipationless) NLS-type models, the experiments show that some patterns persist. This persistence is consistent with recent work by Segur *et al.* (2005) who allowed for damping in the sNLS equation and reconsidered the Benjamin–Feir instability. They showed that any finite amount of damping stabilizes the Stokes wave solution of (damped) sNLS. We conjecture that similar results hold for the stability considerations of the elliptic function solutions of sNLS and the Stokes solution of vNLS.

(xi) We note that the unsteady features described in § 4 are qualitatively reproducible. Their details are not.

The purpose of the above procedure is to determine if standard NLS-type models can describe the features observed in the experiments. Here, we list the features and whether or not they may be described by the models:

(i) *Feature 1: persistence; Feature 2: geometry; Feature 7: Pinch-off of cells; Feature 8: Dips in crestlines; Feature 9: Flattening of crestlines; Feature 12: Curvature of crestlines.* All of these features can be explained by including the travelling-wave solution of the nonlinear Schrödinger equations in a third-order in ϵ expansion of the free-surface displacement as described above.

Feature 1: persistence. By definition, the travelling-wave solutions of the nonlinear Schrödinger equations persist without change of form for all time. Incorporating them into the third-order in ϵ expansion for the free-surface displacement maintains

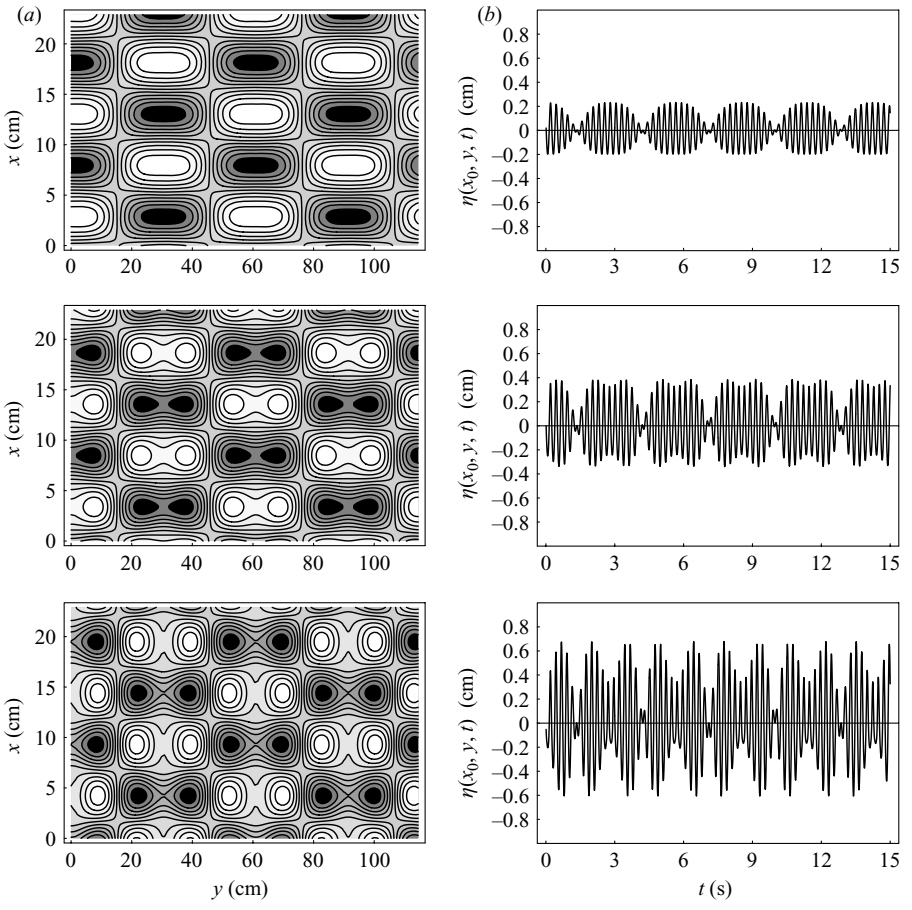

FIGURE 20. (*a*) Contour maps and (*b*) *y*-traces of water surface displacement from computations using the solution for two-phase waves from vNLS in the third-order in ϵ expansion. Parameters in the computations correspond to those of experiments C9 (row 1), C11 (row 2), and C13 (row 3). In (*a*), white regions correspond to troughs and dark regions correspond to crests.

this steadiness. None of the wave fields in the experiments persisted with *no* change of form; but many of the wave fields did persist with a small change in form over the length of our test section. The images of wave fields in the cosine-experiments displayed this qualitative persistence for nonlinearity that was roughtly $a_0\kappa < 0.3$. The Sn-experiments displayed this qualitative persistence for comparable values of nonlinearity.

Features 2: geometry. The procedure listed above uses exact solutions that inherently have a rectangular geometry. Even when the solution for surface displacement is expanded to third order in ϵ, the nodal lines parallel to the x-axis are maintained.

Features 7–9, 12: pinch-off of cells; dips in crestlines; flattening of crestlines; curvature of crestlines. Extending the expansion for free-surface displacement to third-order in ϵ provides an explanation for these four features. For example, consider figure 20, which shows contour maps and y-time traces obtained from the third-order solution that uses the symmetric two-phase wave solution of vNLS and the carrier-wave

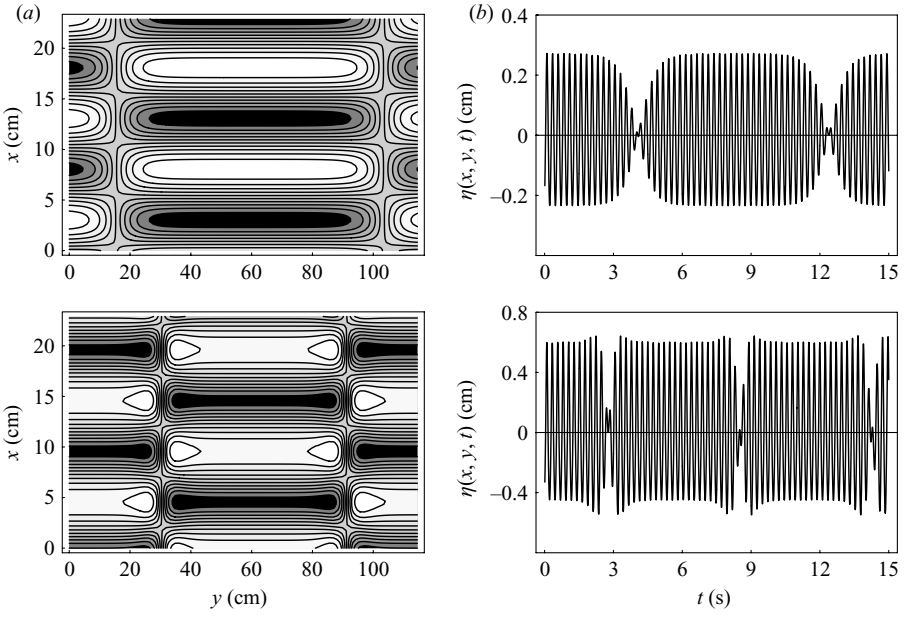

FIGURE 21. (*a*) Contour maps and (*b*) *y*-traces of water surface displacement from computations using the sn-solution of sNLS in the third-order in ϵ expansion. Parameters in the computations correspond to those in table 7 for Snsoln1 (row 1) and Snsoln2 (row 2). In (*a*), white regions correspond to troughs and dark regions correspond to crests.

parameters of experiments C9, C11 and C13. The *y*-time traces show an up/down asymmetry, which is the result of the second-order in ϵ contribution to the solution. This asymmetry is also apparent in the time-series obtained in the data (figure 13). The cubic contributions have an inflection point, which allows the crestlines in the *y*-direction to either flatten or develop a dip in the center. Figure 20 shows the flattening occurred for a value of nonlinearity corresponding to our least nonlinear experiment, C9 ($a_0\kappa = 0.15$), as it did in that experiment. Further increases in nonlinearity result in a dip in the *y*-time series corresponding to a pinch-off in the contour map. This dip has an up/down asymmetry that we do not see in the data shown in figure 13. The theoretical solutions for C11 and C13 show pinch-off and dips. Images from experiments C11 and C13 (figures 8 and 9) did not show pinch-off, but their *y*-time series (figure 13) at $x = 50$ did show dips. (We also note that it is likely that we could use this approach to explain the pinch-off into three cells that appears in the contour map for experiment C2 (figure 6, column II); however, to do so would require a fifth-order expansion in ϵ, which we do not do here.)

Figure 20 also shows that with increasing nonlinearity the crestlines exhibit curvature. This result is consistent with the curvature observed in experiment C14 (figure 9 and additionally in figures 14 and 15).

Computations of the free-surface displacement using the sn-solution of sNLS are qualitatively different from those using the symmetric two-phase wave solution of vNLS. Figure 21 shows computations of the contours of the surface displacement and of the *y*-traces of the surface displacement at a fixed value of *x*. These solutions were chosen to have large values of *m*, corresponding to flattened *y*-crestlines in the first-order in ϵ solution. Row 1 of figure 21 was obtained from computations of the third-order in ϵ solution using Snsoln1 of table 7. The parameters for this solution are

close to those of experiment Sn1 (figure 18); the nonlinearity is $a_0k = 0.16$. Here the y-crestline stayed flat in the third-order in ϵ solution. We note that in the cosine experiments and in the corresponding two-phase solution of vNLS, there were flattened crests for a comparable value of nonlinearity (C9 with $a_0\kappa = 0.15$).

Row 2 of figure 21 was obtained from computations using Snsoln2 of table 7. The parameters for this solution are close to those of experiment Sn2; the nonlinearity is $a_0k = 0.32$. This solution shows pinch-off in the contour map and corresponding dips in the y-crestline. It also shows a nascent curvature of the crestlines in the y-direction. The contour map from experiment Sn2 (figure 16, row 2, column II) shows some evidence of nascent pinch-off, but it is qualitatively different from that of the theoretical solution. Similarly, the y-time series from experiment Sn2 (figure 18*b*, row 2) does show a dip, but it is qualitatively different from that of the solution. The curvature in the crestlines of experiment Sn2 (figure 16) is more pronounced than the small amount shown in figure 21.

Each experiment may be parameterized by its value of nonlinearity and by its aspect ratio. We can use these values, maintaining the y-wavelength of the pattern, to compute solutions using the travelling-wave solution of either sNLS or vNLS for any experiment. Consistent with the above discussion, the resulting third-order in ϵ solutions are qualitatively different in the two cases. Figures 22 and 23 show a comparison of theoretical solutions with two experiments, C14 and Sn5. The first row in both corresponds to the contour map of an image obtained from the experiment and a y-time series obtained from the experiment. The second row corresponds to the third-order symmetric two-phase solution of vNLS (contour map and y-time series) when the amplitude and aspect ratio are taken from the experiment. The third row corresponds to the third-order sn-solution of sNLS (contour map and y-time series), when the amplitude and aspect ratio are taken from the experiment, and the values of m, c and A_0 are computed from (13) and (16) with the additional constraint from maintaining the experimental y-wavelength.

Figure 22 corresponds to experiment C14, the most nonlinear experiment conducted. The experiment (from figure 15*d*, column II and the last row of figure 13*a*) shows both pinch-off and dip(s). The third-order in ϵ solutions for water-surface displacement, using either exact solution show these features also with qualitative differences. The peaks in the crest region are localized near the nodal lines in the sn-solution of sNLS and spread across the anti-nodal region in the 2-phase waves from vNLS. The sizes of the peaks are more pronounced in the 2-phase waves from vNLS than in the sn-solution of sNLS. The first row of figure 22(*a*) shows that the peaks in the experiment are positioned more like those of the 2-phase waves from vNLS but are of a size more similar to those of the sn-solution of sNLS.

Figure 23 corresponds to experiment Sn5. Here, the overhead image of the experiment does not show pinching, but the y-time series does show dips. Using the amplitude and aspect ratio of the cell as the parameters for the solutions of the two model equations, results in a symmetric two-phase wave solution of vNLS that does predict the pinching behaviour and dips. Similarly, the sn-solution of sNLS also predicts these features. The up/down asymmetry in the dips of both solutions for the y-time series is not apparent in the dips in the experimental y-time series. The y-time series from the experiment (first row, column (*b*)), seems to have the signatures of the vNLS solution. In particular, the first full period shows peakedness on either side of the dip that is not as pronounced at the nodal regions as it is in the sNLS solutions; the fourth full period shows a rounded cosine-type shape, consistent with the vNLS solution.

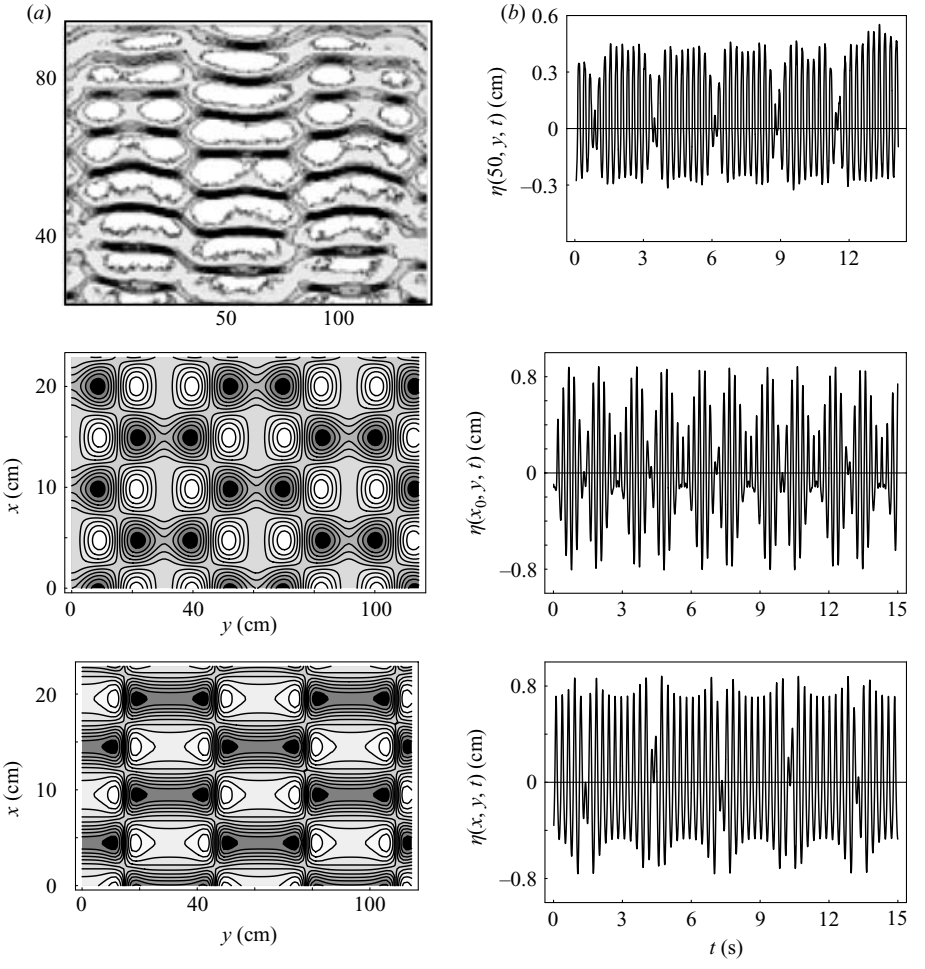

FIGURE 22. (*a*) Contour maps and (*b*) *y*-traces from (row 1) experiment C14; (row 2) third-order calculation of surface displacement using the solution for symmetric two-phase waves from vNLS with the parameters of C14; and (row 3) third-order calculation of surface displacement using the sn-solution of sNLS with the parameters of C1, which give $m = 0.9955$, $|A_0| = 12.34\,\mathrm{cm^2\,s^{-1}}$, and $c = 0.239\,\mathrm{cm^{-1}}$. In the contour maps, white regions correspond to troughs while dark regions correspond to crests.

We note that in these comparisons, the theoretical solutions have larger amplitudes than do the experiments. We note that the values of a_0 listed for the experiments were not measured. They were obtained using results from the (experimental) wavemaker problem in one-dimension as described in § 2. Thus, another approach for comparison is to attempt to fit the solutions to the sets of data obtained at $x = 50\,\mathrm{cm}$.

(ii) *Feature 3: connecting leg between cells; Feature 4: oscillations in the nodal region; Feature 5: modulations in the x-direction; Feature 6: small-scale waves; Feature 10: time-varying width of the nodal region.* These features are all consistent with stability considerations of the exact solutions used here to model the experiments. For example, Aleshkevich *et al.* (2003) and Carter & Segur (2003, hereinafter referred to as CS) found that the Jacobi elliptic sine function solution of sNLS is unstable. Craig *et al.* (personal communication) have found that the Stokes solution of vNLS is unstable.

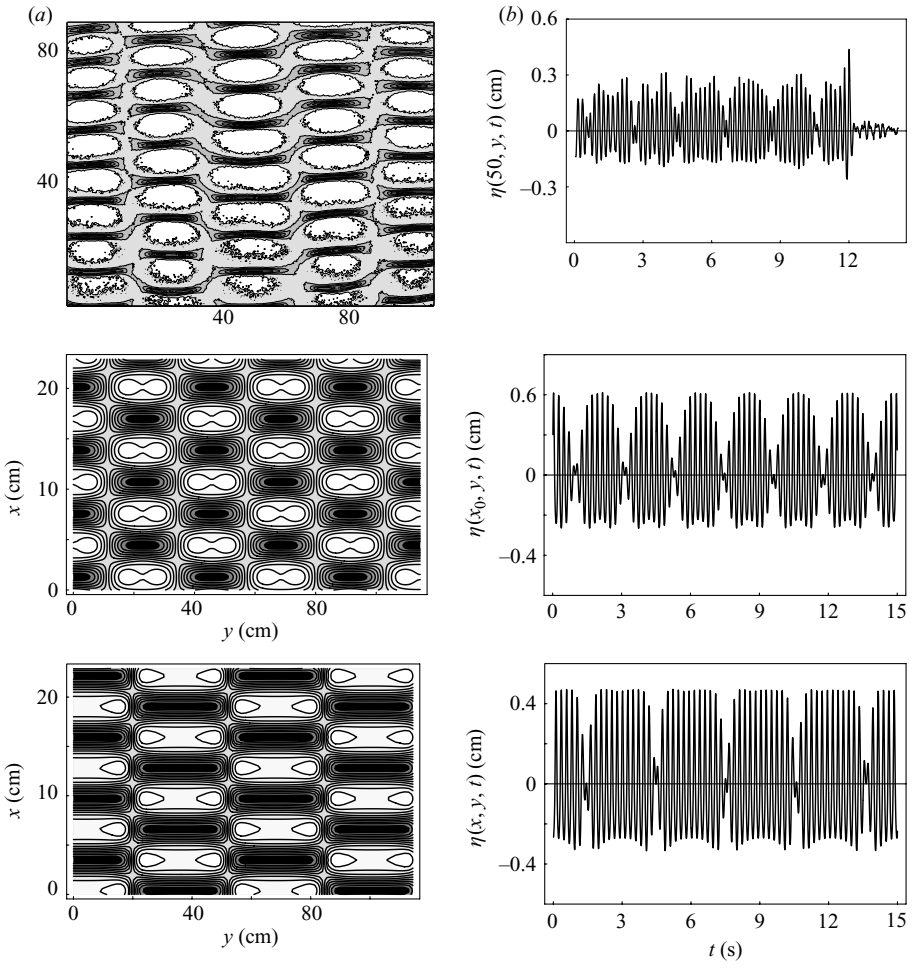

FIGURE 23. (*a*) Contour maps and (*b*) *y*-traces from: (row 1) experiment Sn5; (row 2) third-order calculation of surface displacement using the symmetric two-phase wave solution of vNLS with the parameters of Sn5; and (row 3) third-order calculation of surface displacement using the Sn-solution of sNLS with the parameters of Sn5. In the first row, white regions correspond to troughs while dark regions correspond to crests. In the second and third rows, white regions correspond to crests while dark regions correspond to troughs.

CS showed that two types of instability can occur, corresponding to the 'neck' and 'snake' instabilities discussed by Zakharov & Rubenchik (1974). Here we generalize their definition: a 'neck' mode is an instability with a spatial structure that does not change the location of the nodal lines; a 'snake' mode is an instability with a spatial structure that does change the location of the nodal lines (i.e. causes the nodal lines to oscillate back and forth, like a slithering snake). Thus, a snake mode might explain how oscillations appear and then disappear in the nodal region, as they did in four of the Sn-experiments (Sn1, 2, 3, 5). A neck mode might explain the time-varying width of the nodal lines, as occurred in all of the Sn-experiments to some extent, but is most visible in experiment Sn2. A neck mode might explain the modulations observed in the *x*-direction, as is particularly apparent in experiment Sn5. Combinations of these modes might explain the connecting legs between cells as is also apparent in

the contour map of experiment Sn5. To test these explanations, computations from sNLS that use the pertinent unstable modes along with the carrier wave as input are presently being conducted and compared to the Sn-experiments. The results on stability of the symmetric two-phase wave solution of vNLS, which correspond to the cosine experiments, are also being examined in terms of applications to these experiments. We expect that similar types of instability will explain the analogous features observed in the cosine experiments, and will present results in a separate paper.

The small-scale structures that appeared at an angle to the x-axis in some experiments might be the result of an instability. Carter & Segur (2003) show that an sn-solution of sNLS is unstable to perturbations with arbitrarily short wavelengths. The images of experiments C2–C8 (figures 6 and 7, column I) show small-scale structures that appear at a fairly uniform angle in the crest regions and a different angle in the nodal regions. A detailed comparison of the observations of the small-scale waves and the predictions from Carter & Segur (2003) is underway. The symmetric two-phase wave solution of vNLS is also subject to instabilities with arbitrarily short wavelengths (Craig *et al.* personal communication).

The stability considerations of Carter & Segur (2003) also provide a second explanation for the pinch-off of cells and the dips and flattening of the crestlines in the y-direction. (The first explanation came from using the exact solutions and the third-order in ϵ expansion of water-surface displacement.) Carter (personal communication) used a carrier wave with parameters from table 7 in Appendix B and found multiple unstable modes with the same growth rates. The inclusion of the unstable modes plus the carrier waves at first order in ϵ caused the contour map of the surface displacement to exhibit pinch-off and the y-time series of the surface displacement to exhibit dips as observed in the experiments. Moreover, the calculations with the unstable modes are for an unsteady wave field, which is also consistent with the experimental results.

Despite the instabilities of the exact solutions and their manifestation in the experiments, the patterns, on the whole, persisted; they did not disintegrate. An explanation for persistence is provided by Segur *et al.* (2005), who revisited the Benjamin–Fier instability to account for the presence of damping. They found that any finite amount of damping stabilizes the carrier wave, so that the perturbation may grow, but its amplitude is bounded. We expect to find similar results for the instabilities of the sn-solution of sNLS and the symmetric two-phase wave solution of vNLS. Regardless, the instabilities discussed above have growth rates that increase as the carrier wave increases (holding both the x- and y-wavelengths fixed). Thus, the distance required for an instability to grow large enough to be visible (compared to the length of the wave tank, for example) decreases with increasing carrier wave amplitude. This qualitative relationship is consistent with our experimental results.

(iii) *Feature 11: the zigzag structure.* Neither the travelling-wave solutions nor our present understanding of their instabilities provide explanations for this feature.

(iv) *Feature 12: curving of crestlines in the y-direction.* When nonlinearity is large enough, the third order in ϵ solution using the exact solutions of both sNLS and vNLS do show a curvature of the crests in the y-direction.

5.3. *Summary*

In summary, we have examined two-dimensional surface patterns of progressive waves in deep water, and found that in general, the structure of the patterns persisted in

the length of our tank. This persistence of the spatial structure may have useful consequences in the study and description of deep-water wavetrains.

We generated the patterns using either obliquely interacting wavetrains (C-experiments) or Jacobi elliptic sine functions (Sn-experiments). We conducted twenty experiments that varied aspect ratio and nonlinearity of the cells comprising the pattern and obtained measurements using overhead imaging and wave gauges that provided time series measurements. The patterns generally persisted throughout the length of the wavetank, with some evolution. We listed twelve qualitative features observed in the experiments that characterize the patterns and the evolution. The features that we observed are summarized in table 6 (in § 4), in § 5.2, and below.

To model the patterns and the features, we computed water-surface displacements using either an elliptic function solution of the scalar nonlinear Schrödinger equation or a symmetric two-phase wave solution of vector nonlinear Schrödinger equations in a third-order expansion of the water-wave problem. With these models, we were able to provide explanations for some of the features. Stability considerations provide qualitative explanations for more of the features. We note, however, that Segur *et al.* (2005) showed that dissipation of the type observed in these experiments plays a fundamental role in the stability of deep-water wavetrains. Thus, the stability of the patterns observed here is still an open question.

Below, we list the features observed in the experiments and say whether or not the models presented herein provide qualitative explanations for them.

1. In many parameter regimes, the patterns persisted for the length of the experiment. We chose travelling-wave solutions of the model equations to capture this persistence.

2. Unlike persistent two-dimensional surface patterns in shallow water, which comprise six-sided cells, surface patterns in deep water comprise primarily four-sided cells. We chose exact solutions to the model equations that had this rectangular geometry.

3. In some of the experiments, the contour images showed a non-zero contour connecting two adjacent cells. This connecting leg is inconsistent with a rectangular cell geometry. When it appears in the images, we expect it to appear also as oscillations in the time series obtained in the nodal region, which otherwise would be constant. This correspondence occurred in some experiments, particularly, the Sn-experiments, but not in others, particularly the C-experiments. The connecting leg is not explained by the travelling-wave solutions that we discussed, or the third-order solution for the water surface that used these solutions. Stability considerations of the exact solutions do provide a qualitative explanation for them.

4. Oscillations developed in the nodal regions during some of the experiments, particularly for larger-amplitude experiments and most of the Sn-experments. Again, this result is not consistent with our travelling-wave solutions, but is qualitatively consistent with instabilities of these solutions.

5. Modulations developed in the direction of propagation on some of the patterns. The dominant modulational frequency depended on aspect ratio. Its dependence on nonlinearity was inconsistent with a description that models the wave field as locally one-dimensional. These modulations are not consistent with our travelling-wave solutions, but are qualitatively consistent with instabilities of these solutions.

6. Small-scale waves developed at an angle to the wavemaker in many of the experiments. The origin of these waves is still under investigation. These small-scale waves are not consistent with our travelling-wave solutions, but are qualitatively consistent with instabilities of these solutions.

7. For some of the large-amplitude experiments, the cells may pinch-off in the middle and seem to split into two cells. This pinch-off appears in the images and in the time series taken in they y-direction, as a dip (feature 8). This result is consistent with our travelling-wave solutions when we use them in a third-order expansion of the water-wave problem. However, we note that in the experiments, the pinching was unsteady, while in the travelling-wave models, they are necessarily steady. We can also explain the pinching, as well as its unsteadiness, as an instability of the exact solutions.

8. In many experiments, the shape of the patterns perpendicular to the direction of propagation differed from the shape imposed at the wavemaker. In some experiments, it developed a dip where the peak of a cosine was expected or in the expected flat region of an elliptic function. These dips, which appear as a pinch-off of the cells in the images (feature 7), are consistent with our travelling-wave solutions when we use them in a third-order expansion of the water-wave problem. The dips, as well as their observed unsteadiness, can also be explained as instabilities of the exact solutions.

9. Similarly, in many experiments, the crests perpendicular to the direction of propagation became flat in the C-experiments, when the signal input at the wavemaker had a cosine-shape. This result is also consistent with our travelling wave solution when we use it in a third-order expansion of the water surface displacement. In general, if the input signal is larger, then the propagating wave pattern has more energy in its higher harmonics. The result is that moderate amplitude waves develop a flattening of wave crests across the cell and larger amplitude waves develop a dip in the wave crests in the middle of the cell. Then as the wave propagates, damping removes energy from the fundamental mode and more rapidly from its harmonics so that the y-shape of the wave crest evolves back towards a cosine shape as the overall amplitude decreases. A flat crest was imposed on the Sn-experiments by using an elliptic modulus close to one. A high elliptic modulus corresponds to energy being spread to higher harmonics. So, consistent with the above arguments, in some of these experiments the crests evolved to a cosine-like shape as well.

10. A rectangular cell structure has a nodal-region that is parallel to the axes of propagation. In the center is a line of constant surface displacement. Off that line, there are oscillations with the frequency of the carrier wave and with small amplitudes that increase sharply within a short distance from the nodal line. In some of our experiments, we observed that the width of this nodal-region of constant and small-amplitude oscillatory surface displacements varied in time. This unsteadiness of the width of the nodal-region is not consistent with our travelling-wave solutions, but is qualitatively consistent with instabilities of these solutions.

11. In the most nonlinear experiments, there was a zigzag structure, very similar to the six-sided pattern of shallow-water waves. When these zigzag structures were apparent in the contour maps of overhead images, there were also oscillations in the nodal regions of the patterns. The zigzag structures are not explained by our travelling-wave solutions, or by our current understanding of the stability of these solutions.

12. In some of the experiments the crest-lines parallel to the wavemaker array, curved. This feature is explained by our travelling-wave solutions when used in the third order in ϵ expansion.

While this paper was in press, Joe Hammack, who envisioned the experiments presented herein then designed and built the experimental facility to generate them, passed away. The other two authors: D.H., his wife and colleague, and H.S., his friend and colleague of many years, dedicate this paper to him in loving remembrance.

We thank Walter Craig and Dave Nicholls for figure 4, John Carter, Walter Craig, Bernard Deconinck, Dave Nicholls and Catherine Sulem for helpful conversations, Bob Geist for help building the equipment, and Aaron Naber for doing the contour maps and spatial FFTs of the images. We gratefully acknowledge financial support for this work from Packard and Sloan Fellowships (dmh) and from the National Science Foundation (NSF–DMS 9972210, NSF-DMS–0139847, and NSF–DMS–FRG 0139742).

Appendix A

In this Appendix we list the second and third order in ϵ solutions of water-surface displacement and velocity potential as well as coefficients not spelled out in the text.

The coefficients in the vector nonlinear Schrödinger equations, (22), are given below for $j = 1, 2$. The corresponding coefficients in the scalar nonlinear Schrödinger equation, (8), are obtained from these expressions (with no j-subscript) by setting the y-wavenumber, $l \equiv 0$.

$$\alpha_j = -\frac{1}{2\omega_j}\left[-gh\left[\frac{k_j^2}{\kappa_j^2} + \frac{l_j^2}{\kappa_j^2}\frac{|V_j|\omega_j}{g\kappa_j h}\right] + V_{xj}^2 + \frac{2}{\kappa_j} l_j h\omega_j\sigma_j V_{xj}\right] = \frac{1}{2}\frac{\partial^2\omega_j}{\partial k_j^2}, \tag{A 1}$$

$$\beta_j = -\frac{1}{2\omega_j}\left[-gh\left[\frac{l_j^2}{\kappa_j^2} + \frac{k_j^2}{\kappa_j^2}\frac{|V_j|\omega_j}{g\kappa_j h}\right] + V_{yj}^2 + \frac{2}{\kappa_j} k_j h\omega_j\sigma_j V_{yj}\right] = \frac{1}{2}\frac{\partial^2\omega_j}{\partial l_j^2}, \tag{A 2}$$

$$\gamma_j = -\frac{1}{2\omega_j}\left[\frac{gk_j l_j}{\kappa_j^2}\left[\frac{\sigma_j}{\kappa_j} - h\left(\sigma_j^2 + 1\right)\right] + 2V_{xj}V_{yj} + \frac{2}{\kappa_j} h\omega_j\sigma_j(k_j V_{yj} + l_j V_{xj})\right] = \frac{\partial^2\omega_j}{\partial k_j \partial l_j}, \tag{A 3}$$

$$\xi_j = \frac{\kappa_j^4}{4\omega_j}\left(2\sigma_j^4 - 13\sigma_j^2 + 12 - \frac{9}{\sigma_j^2}\right), \tag{A 4}$$

$$\begin{aligned}
2\omega_j\zeta_j = {} & -2\kappa_j\kappa_m^3\sigma_j\sigma_m + \kappa_j^2\kappa_m^2\left(\sigma_j^2 - 1\right)\left(\sigma_m^2 - 1\right) - 2\frac{\omega_j\omega_m}{g}(k_j k_m + l_j l_m)(2\kappa_m\sigma_m + \kappa_j\sigma_j) \\
& + G\left\{g\left[\kappa_j^2\left(\sigma_j^2 - 1\right) + k_j(k_1 + k_2) + l_j(l_1 + l_2)\right] - \omega_j\kappa_j\sigma_j(\omega_1 + \omega_2)\right\} \\
& + J\left\{g\left[\kappa_j^2\left(\sigma_j^2 - 1\right) \pm k_j(k_1 - k_2) \pm l_j(l_1 - l_2)\right] \mp \omega_j\kappa_j\sigma_j(\omega_1 - \omega_2)\right\} \\
& + \mathrm{i}F\left\{-2\omega_j[k_j(k_1 + k_2) + l_j(l_1 + l_2)] + \kappa_j\kappa_+\sigma_j\sigma_+[(\omega_1 + \omega_2) - \omega_j]\right. \\
& \left. + \omega_j\kappa_+\left[\kappa_+ - \frac{1}{g}(\omega_1 + \omega_2)^2\sigma_+\right] + (\omega_1 + \omega_2)[k_j(k_1 + k_2) + l_j(l_1 + l_2)]\right\} \\
& + \mathrm{i}H\left\{-2\omega_j[k_j(k_1 - k_2) + l_j(l_1 - l_2)] + \kappa_j\kappa_-\sigma_j\sigma_-[(\omega_1 - \omega_2) - \omega_j]\right. \\
& \left. \pm \omega_j\kappa_-\left[\kappa_- - \frac{1}{g}(\omega_1 - \omega_2)^2\sigma_-\right] \pm (\omega_1 - \omega_2)[k_j(k_1 - k_2) + l_j(l_1 - l_2)]\right\}.
\end{aligned} \tag{A 5}$$

Here, the $\pm$ and $\mp$ uses the upper operator for the $j = 1$ solution and the lower operator for the $j = 2$ solution. Finally,

$$\boldsymbol{\chi}_j = \frac{1}{2\omega_j}\left[\kappa_j^2\left(\sigma_j^2 - 1\right)\boldsymbol{V}_j - \omega_j\boldsymbol{\kappa}_j\right]. \tag{A 6}$$

In the above, we use $\sigma_j = \tanh\kappa_j h$, $\sigma_\pm = \tanh[h\kappa_\pm]$, and $\kappa_\pm = \sqrt{(k_1 \pm k_2)^2 + (l_1 \pm l_2)^2}$.

The second-order surface displacement and velocity potential are given by

$$\eta_2(x,y,t) = \frac{h}{g}\sum_{j=1}^{2}\frac{\omega_j\sigma_j}{\kappa_j}\left[k_j\left(\frac{\partial A_j}{\partial X_1}\mathrm{e}^{\mathrm{i}\theta_j}+\frac{\partial A_j^*}{\partial X_1}\mathrm{e}^{-\mathrm{i}\theta_j}\right)+l_j\left(\frac{\partial A_j}{\partial Y_1}\mathrm{e}^{\mathrm{i}\theta_j}+\frac{\partial A_j^*}{\partial Y_1}\mathrm{e}^{-\mathrm{i}\theta_j}\right)\right]$$
$$+\sum_{j=1}^{2}\left[\frac{2\mathrm{i}\omega_j}{g}D_j+\frac{1}{2}\frac{\kappa_j^2}{g}\left(1-3\sigma_j^2\right)\right]\left(A_j^2\mathrm{e}^{2\mathrm{i}\theta_j}+A_j^{*2}\mathrm{e}^{-2\mathrm{i}\theta_j}\right)$$
$$+\sum_{j=1}^{2}\frac{\kappa_j^2}{g}\left(\sigma_j^2-1\right)|A_j|^2-\frac{1}{g}\frac{\partial\Phi_1}{\partial T_1}-\frac{1}{g}\sum_{j=1}^{2}\left(\frac{\partial A_j}{\partial T_1}\mathrm{e}^{\mathrm{i}\theta_j}+\frac{\partial A_j^*}{\partial T_1}\mathrm{e}^{-\mathrm{i}\theta_j}\right)$$
$$+G\left(A_1A_2\mathrm{e}^{\mathrm{i}(\theta_1+\theta_2)}+A_1^*A_2^*\mathrm{e}^{-\mathrm{i}(\theta_1+\theta_2)}\right)+J\left(A_1A_2^*\mathrm{e}^{\mathrm{i}(\theta_1-\theta_2)}+A_1^*A_2\mathrm{e}^{-\mathrm{i}(\theta_1-\theta_2)}\right),$$

$$\phi_2(x,y,z,t) = \Phi_2-\mathrm{i}(z+h)\sum_{j=1}^{2}\frac{\sinh\kappa_j(z+h)}{\kappa_j\cosh\kappa_jh}\left[k_j\left(\frac{\partial A_j}{\partial X_1}\mathrm{e}^{\mathrm{i}\theta_j}-\frac{\partial A_j^*}{\partial X_1}\mathrm{e}^{-\mathrm{i}\theta_j}\right)\right.$$
$$\left.+l_j\left(\frac{\partial A_j}{\partial Y_1}\mathrm{e}^{\mathrm{i}\theta_j}-\frac{\partial A_j^*}{\partial Y_1}\mathrm{e}^{-\mathrm{i}\theta_j}\right)\right]+\sum_{j=1}^{2}D_j\frac{\cosh 2\kappa_j(z+h)}{\cosh 2\kappa_jh}\left(A_j^2\mathrm{e}^{2\mathrm{i}\theta_j}-A_j^{*2}\mathrm{e}^{-2\mathrm{i}\theta_j}\right)$$
$$+F\frac{\cosh[(z+h)\kappa_+]}{\cosh[h\kappa_+]}\left(A_1A_2\mathrm{e}^{\mathrm{i}(\theta_1+\theta_2)}-A_1^*A_2^*\mathrm{e}^{-\mathrm{i}(\theta_1+\theta_2)}\right)$$
$$+H\frac{\cosh[(z+h)\kappa_-]}{\cosh[h\kappa_-]}\left(A_1A_2^*\mathrm{e}^{\mathrm{i}(\theta_1-\theta_2)}-A_1^*A_2\mathrm{e}^{-\mathrm{i}(\theta_1-\theta_2)}\right), \tag{A 7}$$

where

$$\theta_j=\boldsymbol{\kappa}_j\cdot(x,y)-\omega_jt.$$

For computing solutions using the exact solution to sNLS, A_2 and its derivatives are all zero. The coefficients are

$$D_j=\tfrac{3}{4}\mathrm{i}\frac{\omega_j\kappa_j}{g}\left(\frac{1-\sigma_j^4}{\sigma_j^3}\right), \tag{A 8}$$

$$G=-\frac{\omega_1\omega_2}{g^2}(\kappa_1\sigma_1+\kappa_2\sigma_2)+\frac{1}{g}(k_1k_2+l_1l_2)-\frac{1}{g}\kappa_1\kappa_2\sigma_1\sigma_2+\frac{\mathrm{i}}{g}F(\omega_1+\omega_2), \tag{A 9}$$

$$J=\frac{\omega_1\omega_2}{g^2}(\kappa_1\sigma_1+\kappa_2\sigma_2)-\frac{1}{g}(k_1k_2+l_1l_2)-\frac{1}{g}\kappa_1\kappa_2\sigma_1\sigma_2+\frac{\mathrm{i}}{g}H(\omega_1-\omega_2), \tag{A 10}$$

$$F=\mathrm{i}\frac{2(\omega_1+\omega_2)[\kappa_1\kappa_2\sigma_1\sigma_2-(k_1k_2+l_1l_2)]+\omega_1\kappa_2^2\left(\sigma_2^2-1\right)+\omega_2\kappa_1^2\left(\sigma_1^2-1\right)}{g\sigma_+\kappa_+-(\omega_1+\omega_2)^2}, \tag{A 11}$$

$$H=\mathrm{i}\frac{2(\omega_1-\omega_2)[\kappa_1\kappa_2\sigma_1\sigma_2+(k_1k_2+l_1l_2)]+\omega_1\kappa_2^2\left(\sigma_2^2-1\right)-\omega_2\kappa_1^2\left(\sigma_1^2-1\right)}{g\sigma_-\kappa_--(\omega_1-\omega_2)^2}. \tag{A 12}$$

The third-order velocity potential is

$$\phi_3=\Phi_3-\tfrac{1}{2}(z+h)^2\left(\frac{\partial^2\Phi_1}{\partial X_1^2}+\frac{\partial^2\Phi_1}{\partial Y_1^2}\right)-2\mathrm{i}(z+h)\sum_{j=1}^{2}D_j\frac{\sinh 2\kappa_j(z+h)}{\kappa_j\cosh 2\kappa_jh}$$
$$\times\left[k_j\left(A_j\frac{\partial A_j}{\partial X_1}\mathrm{e}^{2\mathrm{i}\theta_j}+\text{c.c.}\right)+l_j\left(A_j\frac{\partial A_j}{\partial Y_1}\mathrm{e}^{2\mathrm{i}\theta_j}+\text{c.c.}\right)\right]$$

$$
\begin{aligned}
&-\sum_{j=1}^{2}\left[\tfrac{1}{2}(z+h)^2\frac{k_j^2}{\kappa_j^2}\frac{\cosh\kappa_j(z+h)}{\cosh\kappa_j h}+\frac{1}{2\kappa_j}(z+h)\frac{l_j^2}{\kappa_j^2}\frac{\sinh\kappa_j(z+h)}{\cosh\kappa_j h}\right]\left(\frac{\partial^2 A_j}{\partial X_1^2}\mathrm{e}^{\mathrm{i}\theta_j}+\text{c.c.}\right)\\
&-\sum_{j=1}^{2}\left[\tfrac{1}{2}(z+h)^2\frac{l_j^2}{\kappa_j^2}\frac{\cosh\kappa_j(z+h)}{\cosh\kappa_j h}+\frac{1}{2\kappa_j}(z+h)\frac{k_j^2}{\kappa_j^2}\frac{\sinh\kappa_j(z+h)}{\cosh\kappa_j h}\right]\left(\frac{\partial^2 A_j}{\partial Y_1^2}\mathrm{e}^{\mathrm{i}\theta_j}+\text{c.c.}\right)\\
&+\sum_{j=1}^{2}\left[-\frac{k_j l_j}{\kappa_j^2}(z+h)^2\frac{\cosh\kappa_j(z+h)}{\cosh\kappa_j h}+\frac{k_j l_j}{\kappa_j^3}(z+h)\frac{\sinh\kappa_j(z+h)}{\cosh\kappa_j h}\right]\\
&\times\left(\frac{\partial^2 A_j}{\partial X_1\partial Y_1}\mathrm{e}^{\mathrm{i}\theta_j}+\text{c.c.}\right)-\mathrm{i}F(z+h)\left(\frac{k_1+k_2}{\kappa_+}\right)\frac{\sinh[\kappa_+(z+h)]}{\cosh[\kappa_+ h]}\\
&\times\left[\left(\frac{\partial A_1}{\partial X_1}A_2\mathrm{e}^{\mathrm{i}(\theta_1+\theta_2)}+\text{c.c.}\right)+\left(A_1\frac{\partial A_2}{\partial X_1}\mathrm{e}^{\mathrm{i}(\theta_1+\theta_2)}+\text{c.c.}\right)\right]\\
&-\mathrm{i}F(z+h)\left(\frac{l_1+l_2}{\kappa_+}\right)\frac{\sinh[\kappa_+(z+h)]}{\cosh[\kappa_+ h]}\left[\left(\frac{\partial A_1}{\partial Y_1}A_2\mathrm{e}^{\mathrm{i}(\theta_1+\theta_2)}+\text{c.c.}\right)\right.\\
&\left.+\left(A_1\frac{\partial A_2}{\partial Y_1}\mathrm{e}^{\mathrm{i}(\theta_1+\theta_2)}+\text{c.c.}\right)\right]-\mathrm{i}H(z+h)\left(\frac{k_1-k_2}{\kappa_-}\right)\frac{\sinh[\kappa_-(z+h)]}{\cosh[\kappa_- h]}\\
&\times\left[\left(\frac{\partial A_1}{\partial X_1}A_2^*\mathrm{e}^{\mathrm{i}(\theta_1-\theta_2)}+\text{c.c.}\right)+\left(A_1\frac{\partial A_2^*}{\partial X_1}\mathrm{e}^{\mathrm{i}(\theta_1-\theta_2)}+\text{c.c.}\right)\right]-\mathrm{i}H(z+h)\left(\frac{l_1-l_2}{\kappa_-}\right)\\
&\times\frac{\sinh[\kappa_-(z+h)]}{\cosh[\kappa_- h]}\left[\left(\frac{\partial A_1}{\partial Y_1}A_2^*\mathrm{e}^{\mathrm{i}(\theta_1-\theta_2)}+\text{c.c.}\right)+\left(A_1\frac{\partial A_2^*}{\partial Y_1}\mathrm{e}^{\mathrm{i}(\theta_1-\theta_2)}+\text{c.c.}\right)\right]\\
&+\sum_{j=1}^{2}M_j\frac{\cosh 3\kappa_j(z+h)}{\cosh 3\kappa_j h}\left(A_j^3\mathrm{e}^{3\mathrm{i}\theta_j}+\text{c.c.}\right)+P\frac{\cosh\kappa_{(2+1)}(z+h)}{\cosh\kappa_{(2+1)}h}\left(A_1^2A_2\mathrm{e}^{\mathrm{i}(2\theta_1+\theta_2)}+\text{c.c.}\right)\\
&+R\frac{\cosh\kappa_{(2-1)}(z+h)}{\cosh\kappa_{(2-1)}h}\left(A_1^2A_2^*\mathrm{e}^{\mathrm{i}(2\theta_1-\theta_2)}+\text{c.c.}\right)\\
&+Q\frac{\cosh\kappa_{(1+2)}(z+h)}{\cosh\kappa_{(1+2)}h}\left(A_1A_2^2\mathrm{e}^{\mathrm{i}(\theta_1+2\theta_2)}+\text{c.c.}\right)\\
&+S\frac{\cosh\kappa_{(1-2)}(z+h)}{\cosh\kappa_{(1-2)}h}\left(A_1A_2^{*2}\mathrm{e}^{\mathrm{i}(\theta_1-2\theta_2)}+\text{c.c.}\right),
\end{aligned}
\tag{A 13}
$$

where c.c. indicates complex conjugate and $\kappa_{(n\pm m)}=\sqrt{(nk_1\pm mk_2)^2+(nl_1\pm ml_2)^2}$. The terms before the one starting with M_j are the solutions to the inhomogeneous part of Laplace's equation at third-order. They satisfy the third-order boundary conditions, and the coefficients are given above. The remaining terms satisfy the homogeneous Laplace's equation. They are not required for the derivation of vNLS, but are required to calculate the third-order water-surface displacement. Therefore, we computed these coefficients only for the case of symmetric deep-water waves, in order to compare with our experiments, which are in that regime.

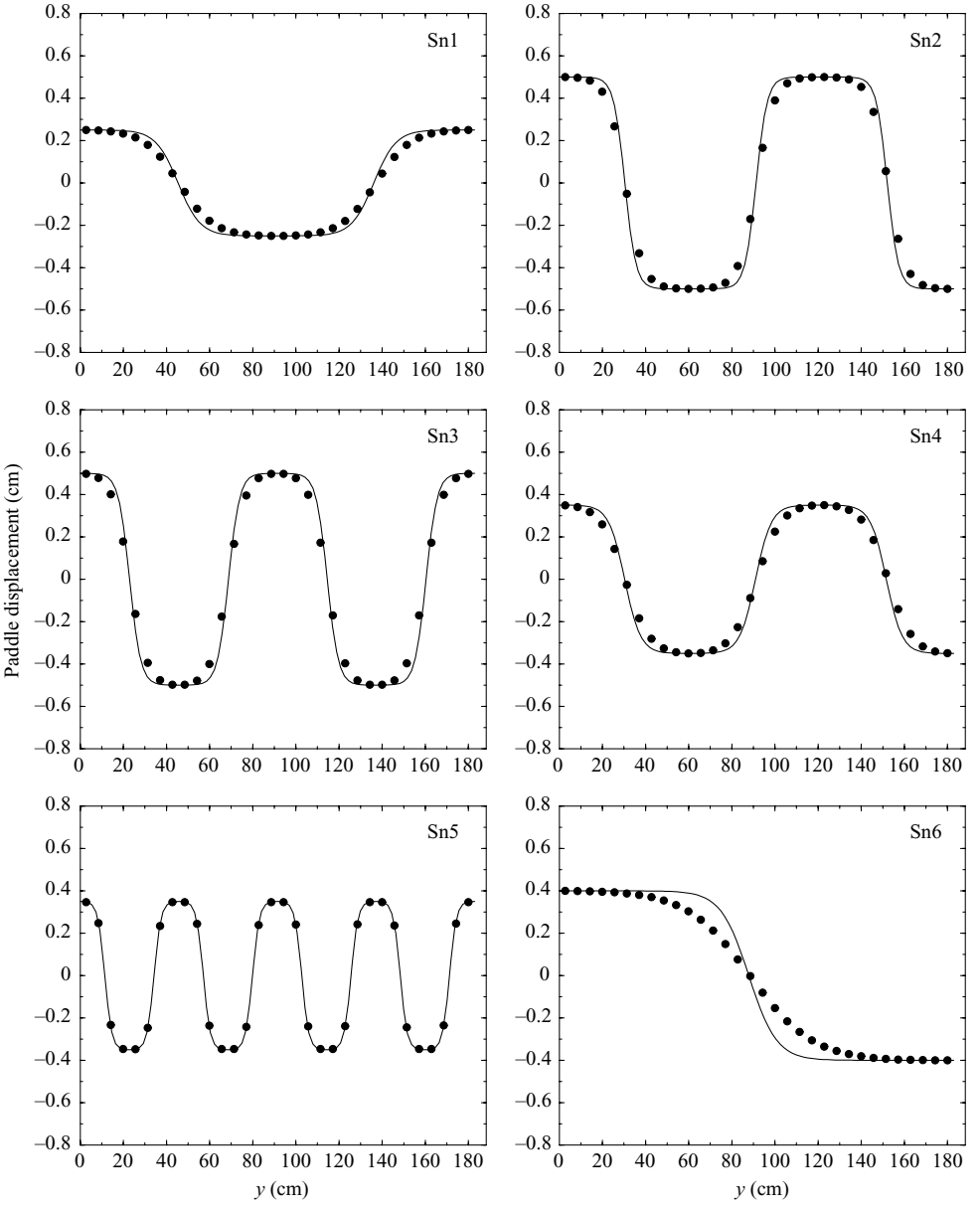

FIGURE 24. Amplitudes divided by C as explained in the text. ●, forcing amplitudes for the corresponding wave paddles as given by (2) with $x = t = 0$ and parameters given in table 3; —, exact solutions of sNLS, corresponding to (15) with $x = t = 0$ and parameters given in table 7.

For the case of two symmetric deep-water waves, as defined in § 5.1,

$$M_j \equiv 0; \qquad j = 1, 2,$$

$$P \equiv Q = \frac{-k^5 - 82k^3l^2 - 85kl^4 + 2k^4\kappa + 60k^2l^2\kappa + 26l^4\kappa}{(k - 2\kappa)[-(3\omega)^2 + g\sqrt{(3k)^2 + l^2}]},$$

$$R \equiv S = \frac{-2\kappa^2(k^2 + 2\kappa^2)}{-\omega^2 + g\sqrt{k^2 + (3l)^2}}. \tag{A 14}$$

Exp	f (Hz)	a_0 (cm)	c/k	$\lvert A_0\rvert(k^2/\sqrt{gk})$	m	$\omega_s/\sqrt{gk}$
Snsoln1	4.00	0.25	0.16	0.080	0.9988	−0.013
Snsoln2	4.00	0.50	0.32	0.16	0.99994	−0.051
Snsoln3	4.00	0.50	0.32	0.16	0.9989	−0.051
Snsoln4	4.00	0.35	0.22	0.11	0.9979	−0.025
Snsoln5	5.00	0.35	0.35	0.18	0.9931	−0.062
Snsoln6	3.33	0.40	0.18	0.089	0.99999	−0.016

TABLE 7. Parameters for the exact solution (12) of sNLS that is near the forcing for experiments Sn1-6 given in table 3. (The x-wavenumber, k, is given in table 3).

The third-order water-surface displacement is found from the inhomogeneous dynamic free-surface boundary condition at third order. So,

$$\eta_3 = -\frac{1}{g}\left(\frac{\partial\phi_3}{\partial t}\right) - \frac{1}{g}\left[\frac{\partial^2\phi_2}{\partial t\partial z}\eta_1 + \frac{\partial^2\phi_1}{\partial t\partial z}\eta_2 + \frac{1}{2}\frac{\partial^3\phi_1}{\partial z^2\partial t}\eta_1^2 + \frac{\partial\phi_1}{\partial x}\left(\frac{\partial\phi_2}{\partial x} + \frac{\partial^2\phi_1}{\partial z\partial x}\eta_1\right)\right.$$
$$+ \frac{\partial\phi_1}{\partial y}\left(\frac{\partial\phi_2}{\partial y} + \frac{\partial^2\phi_1}{\partial z\partial y}\eta_1\right) + \frac{\partial\phi_1}{\partial z}\left(\frac{\partial\phi_2}{\partial z} + \frac{\partial^2\phi_1}{\partial z^2}\eta_1\right) + \frac{\partial\phi_2}{\partial T_1} + \frac{\partial^2\phi_1}{\partial T_1\partial z}\eta_1$$
$$\left. + \frac{\partial\phi_1}{\partial X_1}\frac{\partial\phi_1}{\partial x} + \frac{\phi_1}{\partial Y_1}\frac{\partial\phi_1}{\partial y} + \frac{\partial\phi_1}{\partial T_2}\right],$$

where derivatives with respect to T_2 are required at this order of ϵ for a single carrier wave ($j = 1$), but not for multiple carrier waves ($j = 1, 2$).

Appendix B

Exact solutions of sNLS that have parameters close to those of the Sn-experiments are described in table 7. They use the experiments' carrier wave amplitudes, x-wavenumbers, k, and number of nodal lines. Specifying the number of nodal lines and the carrier wave amplitude fixes the elliptic modulus, m, the y-wavenumber, c, and the amplitude $|A_0|$. The y-wavenumber and frequency correction are computed from (13) and (14). Comparisons between the wave paddle forcing used in the Sn-experiments and these exact solutions are shown in figure 24.

REFERENCES

ABLOWITZ, M. J. & SEGUR, H. 1981 *Solitons and the Inverse Scattering Transform*. SIAM Studies in Applied Mathematics, vol. 4, Philadelphia, PA, 425pp.

ALESHKEVICH, V. A., EGOROV, A. A., KARTASHOV, Y. V., VYSLOUKH, V. A. & ZELENINA, A. S. 2003 Stability analysis of spatiotemporal cnoidal waves in cubic nonlinear media. *Phys. Rev.* E **67**, 066605.

BENJAMIN, T. B. & FEIR, J. E. 1967 The disintegration of wavetrains on deep water. *J. Fluid Mech.* **27**, 417–430.

BENNEY, D. J. & NEWELL, A. C. 1967 The propagation of nonlinear wave envelopes. *J. Maths Phys.* **46**, 133–139.

BRIDGES, T. J., DIAS, F. & MENASCE, D. 2001 Steady three-dimensional water-wave patterns on a finite-depth fluid. *J. Fluid Mech.* **436**, 145–175.

BRYANT, P. J. 1985 Doubly periodic progressive permanent waves in deep water. *J. Fluid Mech.* **161**, 27–42.

BYRD, P. & FRIEDMAN, M. D. 1971 *Handbook of Elliptic Integrals for Engineers and Scientists*. Springer.

Carter, J. 2001 *Stability and Existence of Traveling Wave Solutions of the Two-Dimensional Nonlinear Shcrödinger Equation and its Higher-Order Generalizations*. PhD thesis, University of Colorado at Boulder.

Carter, J. & Segur, H. 2003 Instabilities in the two-dimensional cubic nonlinear Schrödinger equation. *Phys. Rev.* E **68**, 045601:1–4.

Caulliez, G. & Collard, F. 1999 Three-dimensional evolution of wind waves from gravity–capillary to short gravity range. *Eur. J. Mech.* B/*Fluids* **18**, 389–402.

Caulliez, G., Ricci, N. & Dupont, R. 1998 The generation of the first visible wind waves. *Phys. Fluids* **10**, 757–759.

Collard, F. & Caulliez, G. 1999 Oscillating crescent-shaped water wave patterns. *Phys. Fluids* **11**, 3195–3197.

Craig, W. & Nicholls, D. 2000 Traveling two and three dimensional capillary gravity water waves. SIAM: *Math. Anal.* **32**, 323–359.

Craig, W. & Nicholls, D. 2002 Traveling gravity water waves in two and three dimensions. *Euro. J. Mech.* B/*Fluids* **21**, 615–641.

Davey, A. & Stewartson, K. 1974 On three-dimensional packets of surface waves. *Proc. R. Soc. Lond.* A **338**, 101–110.

Dias, F. & Härăgus-Courcelle, M. 2000 On the transition from two-dimensional to three-dimensional water waves. *Stud. Appl. Maths* **104**, 91–127.

Dias, F. & Kharif, C. 1999 Nonlinear gravity and capillary–gravity waves. *Annu. Rev. Fluid Mech.* **31**, 301–346.

Djordjevic, V. D. & Redekopp, L. G. 1977 On two-dimensional packets of capillary gravity waves. *J. Fluid Mech.* **79**, 703–714.

Hammack, J. & Henderson, D. 2003 Experiments on deep-water waves with two-dimensional surface patterns. *J. Offshore Mech. Arctic Engng Special issue: J.V. Wehausen Symposium on Water Waves, Ship Waves, and Marine Hydrodynamics* **125**, 48–53.

Hammack, J., McAllister, D., Scheffner, N. & Segur, H. 1995 Two-dimensional periodic waves in shallow water. Part 2. Asymmetric waves. *J. Fluid Mech.* **285**, 95–122.

Hammack, J., Scheffner, N. & Segur, H. 1989 Two-dimensional periodic waves in shallow water. *J. Fluid Mech.* **209**, 567–589.

Hammack, J., Scheffner, N. & Segur, H. 1991 A note on the generation and narrowness of periodic rip currents. *J. Geophys. Res.* **96**, 4909–4914.

Kimmoun, O., Branger, H. & Kharif, C. 1999 On short-crested waves: experimental and analytical investigations. *Eur. J. Mech.* B/*Fluids* **18**, 889–930.

Lucassen-Reynders, E. H. & Lucassen, J. 1969 Properties of capillary waves. *Adv. Colloid Interface Sci.* **2**, 347–395.

Liu, X. & Duncan, J. H. 2003 The effects of surfactants on spilling breaking waves. *Nature* **421**, 520–524.

Miles, J. W. 1967 Surface-wave damping in closed basins. *Proc. R. Soc.* A **297**, 459–475.

Musslimani, Z. H. & Yang, J. 2001 Transverse instability of strongly coupled dark–bright Manakov vector solitons. *Optics Lett.* **26**, 1981–1983.

Nicholls, D. P. 1998 Traveling water waves: spectral continuation methods with parallel implementation. *J. Comput. Phys.* **143**, 224–240.

Perlin, M. & Hammack, J. 1991 Experiments on ripple instabilities. Part 3. Resonant quartets of the Benjamin–Feir type. *J. Fluid Mech.* **229**, 229–268.

Pierce, R. D. & Knobloch, E. 1994 On the modulational stability of traveling and standing water waves. *Phys. Fluids* **6**, 1177–1190.

Pierce, R. D. & Wayne, C. E. 1995 On the validity of mean-field amplitude equations for counterpropagating wavetrains. *Nonlinearity* **8**, 769–779.

Pritt, T. D. 2003 Linear wavemaker problem for triangular and exponentially shaped wavemakers. MA thesis, Pennsylvania State University.

Roberts, A. J. 1983 Highly nonlinear short-crested water waves. *J. Fluid Mech.* **135**, 301–321.

Roberts, A. J. & Peregrine, D. H. 1983 Notes on long-crested water waves. *J. Fluid Mech.* **135**, 323–335.

Roberts, A. J. & Schwartz, L. W. 1983 The calculation of nonlinear short-crested gravity waves. *Phys. Fluids* **26**, 2388–2392.

Segur, H. & Finkel, A. 1985 An analytical model of periodic waves in shallow water. *Stud. Appl. Maths* **73**, 183–220.

Segur, H., Henderson, D. M., Carter, J., Hammack, J. L., Li, C.-M., Pheiff, D. & Socha, K. 2005 Stabilizing the Benjamin–Feir instability. *J. Fluid Mech.* (to appear).

Stokes, G. G. 1847 On the theory of oscillatory waves. *Trans. Camb. Phil. Soc.* **8**, and Supplement. *Scientific Papers*, **1**.

Su, M.-Y. 1982 Three-dimensional deep-water waves. Part 1. Experimental measurement of skew and symmetric wave patterns. *J. Fluid Mech.* **124**, 73–108.

Su, M.-Y., Bergin, M., Marler, P. & Myrick, R. 1982 Experiments on nonlinear instabilites and evolution of steep gravity-wave trains. *J. Fluid Mech.* **124**, 45–72.

Whitham, G. B. 1967 Nonlinear dispersion of water waves. *J. Fluid Mech.* **27**, 399–412.

Zakharov, V. E. 1968 Stability of periodic waves of finite amplitude on the surface of a deep fluid. *J. Appl. Mech. Tech. Phys.* **2**, 190–194.

Zakharov, V. E. & Rubenchik, A. M. 1974 Instability of wave guides and solitons. *Sov. Phys. JETP* **38** (3), 494–500.